Hindawi
International Journal of Antennas and Propagation
Volume 2020, Article ID 7169846, 23 pages
https://doi.org/10.1155/2020/7169846

Research Article

Quad-Band 3D Rectenna Array for Ambient RF Energy Harvesting

Fatima Khalid, Warda Saeed, Nosherwan Shoaib, Muhammad U. Khan, and Hammad M. Cheema

Research Institute for Microwave and Millimeter-Wave Studies (RIMMS), National University of Sciences and Technology (NUST), Islamabad, Pakistan

Correspondence should be addressed to Nosherwan Shoaib; nosherwan.shoaib@seecs.edu.pk

Received 19 January 2020; Revised 23 March 2020; Accepted 8 April 2020; Published 15 May 2020

Academic Editor: Hervé Aubert

This paper presents a quad-band, 3D mountable rectenna module for ambient energy harvesting. With the aim of powering up Internet of Things (IoT) nodes in practical ambient environments, a hybrid approach of combining power, both at RF and DC, is adopted using 98 MHz FM band, GSM900 (Global System for Mobile Communications), GSM1800, and Wi-Fi 2.4 GHz band. A dual polarized cross-dipole antenna featuring asymmetric slots as well as central ring structure enables multiband response and improved matching at the higher three frequency bands, whereas a loaded monopole wire antenna is used at the lower FM band. Four identical multiband antennas are placed in a 3D cubic arrangement that houses a 4-to-1 power combiner and matching circuits on the inside and the FM antenna on the top. In order to maintain stable rectenna output at varying input power levels and load resistances, a novel transmission line based matching network using closed form equations is proposed. Integrated in form of a $10 \times 10 \times 10\,cm^3$ cube using standard FR4 substrate, the rectenna generates a peak output voltage of 2.38 V at −10 dBm input power. The RF to DC conversion efficiency is 70.28%, 41.7%, 33.37%, and 27.69% at 98 MHz, 0.9 GHz, 1.8 GHz, and 2.4 GHz, respectively, at −6 dBm. The rectenna also exhibits a measured conversion efficiency of 31.3% at −15 dBm for multitone inputs in ambient environment. The promising results in both indoor and outdoor settings are suitable to power low power IoT devices.

1. Introduction

Recent advancements in the field of Internet of Things (IoT) have triggered the "smart" wave, be it homes, offices, factories, automobiles, manufacturing, transportation, logistics, healthcare, agriculture, and environment. Billions of Internet enabled IoT nodes deployed across the globe, gather, monitor, and exchange data thereby providing actionable information to the end-users. Efficient powering of these nodes is a major challenge as, many a time, they cannot be connected to the grid due to their operating environments and spatial distribution. Batteries that are currently used to power sensor nodes need constant maintenance, are disposal, and are difficult to deploy and replace in remote and inaccessible areas. Hence, charging of batteries wirelessly or designing completely battery free systems has become key research challenges.

Energy harvesting offers an interesting solution for powering IoT devices by utilizing energy available in the natural environment. Technologies like solar, thermal, piezoelectric, and Radio Frequency (RF) energy harvesting have become potential alternatives to enable self-sustainability in sensor nodes. RF energy harvesting offers a number of advantages over others due to its constant availability, smaller size, and independence from environmental and mechanical constraints. Energy gathered from the radio frequency band (3000 Hz–300 GHz) can be utilized to operate low power electronic devices; however, large scale deployment of RF energy harvesting systems has remained elusive to date.

A large body of published works is available on RF energy harvesting. Applications such as prototype aerial vehicles [1], remote sensing nodes [2], and medical implants [3] have been demonstrated using RF energy harvesting, albeit using large dedicated and controlled power sources. This not only increases the expense of the overall system but also limits the applications of energy harvesting. On the contrary harvesting energy from ambient sources can truly

realize the concept of "energy on the go" and is expected to reduce system costs as well as improve portability; however, it poses serious design challenges.

The basic driver for harvesting energy is a rectenna that comprises an antenna and a rectifier. An impedance matching network is added before the rectifier to ensure maximum power transfer between the antenna and load. The overall RF-DC conversion efficiency is the key parameter to evaluate the performance of a rectenna. A number of single-band, multiband, and broadband rectennas have been published in literature. Some single-band rectennas have achieved high conversion efficiencies in access of 60%; however, they have a narrowband response and operate at high input power levels (e.g., 0 dBm [4], 5 dBm [5], 10 dBm [6]), 15 dBm [7], 18 dBm [8], and 20 dBm [9]). The average signal strength of EM waves in the environment is around −15 to −30 dBm, making these designs unsuitable for ambient energy harvesting. Therefore, multiband and broadband rectennas are preferred so that more energy can be harvested. For instance, [10] proposes a cross-dipole antenna that can harvest energy from six bands including DTV and most of the communication bands; however, it does not utilize the FM band. Similarly, [11] uses a differentially fed slot antenna with a reflector to enhance gain and harvest energy from three bands. A codesigned rectenna, which eliminates the need of a matching network by modifying the receiving dipole antenna, is presented in [12], whereas [13] proposes a stacked quad-band rectenna with an efficiency of up to 84%. A rectenna with embedded harmonic filter to reject higher order harmonics generated by the nonlinear rectifier is presented in [14]. Design of multiband and broadband rectennas is challenging due to the dependence of input and load impedance on multiple frequencies and a stable design for all frequencies and input power levels is extremely challenging to achieve. Most of the above reported designs exhibit high efficiencies for a narrow range of input power and gather energy from a single direction only.

FM frequency band is also a potential harvesting source due to its wide availability, lower path loss, and simpler circuit design. There are very few published designs that harvest energy from this band. References [15, 16] have proposed rectennas operating in the FM band using a loop antenna with diameter (0.81λ) and a whip antenna, respectively. Reference [17] demonstrated a wideband FM rectenna harvesting from nearly 23% of the available FM band. However, the total size of the antenna is nearly $1 \times 0.59\,\text{m}^2$, which is quite large to be of any use in small IoT applications. Use of FM band in energy harvesting is limited due to the large antenna size, miniaturizing, which degrades its performance in terms of gathering usable amount of energy from environment. Thus harvesting from this band has not become mainstream.

A major challenge in the design of a multiband rectenna is the impedance matching network. As the rectifier is inherently a nonlinear device, its input impedance is a function of frequency, input power level, and load impedance. Hence designing an impedance matching network having good performance at varying frequencies and input power is very important. Most of the existing multiband rectennas use lumped element matching, which is lossy and cannot be implemented at higher frequencies. Few transmission line (TL) based matching designs have also been reported in literature. For instance [18] proposes dual band rectifier using transmission lines operating at 14.2 dBm input power. References [19, 20] propose quad-band rectifier designs operating at an input power range of −12 dBm to 12 dBm and −5 dBm, respectively. All these designs are operating on power levels that are higher than the ambient power levels, whereas for ambient energy harvesting, power levels are expected to vary depending upon time and location. Moreover, the matching network in [18] is designed for 14.2 dBm power level only. Therefore, a matching network is required whose initial parameter values can be calculated using much simpler closed form equations and then these values can be optimized to cover the entire range of ambient power levels. Moreover, the proposed triband matching network is an extension of the dual band matching network reported in [21], which could only be used for two frequency bands.

In this paper a three-dimensional (3D) multiband rectenna with a novel impedance matching network is presented. The rectenna uses four multiband antennas covering GSM900, GSM1800, and 2.4 GHz with combined RF output fed to the rectifier. The matching network has been designed using closed form equations for input power levels as low as −30 dBm. A separate FM rectenna has been designed at 98 MHz and integrated with the multiband rectenna using DC combination of the rectifier outputs. The simulated conversion efficiency of the triband and FM rectifier is up to 77% and 80%, respectively, at −6 dBm input power. To the best of the author's knowledge, the proposed design is the first to harvest energy from FM (98 MHz), GSM900, GSM1800, and 2.4 GHz (Wi-Fi) bands simultaneously.

The paper is organized as follows: Section 2 introduces the proposed concept of energy harvesting at a system level. Section 3 discusses the survey of ambient RF energy in test environment. The antenna design for multiband and FM energy harvesting is discussed in Section 4. Sections 5 and 6 discuss the design of the multiband rectifier and matching network, respectively. Experimental results of rectenna including indoor and outdoor measurements are presented in Section 7 followed by the conclusions in Section 8.

2. System Level Concept

Multiple rectenna array architectures have been studied in literature that aim to enhance harvested energy. Array rectennas use either RF combination of the antenna outputs or DC combination of multiple rectifier outputs. The former, shown in Figure 1(a), increases the power by combining the received RF power before rectification. In this case, rectifiers require larger breakdown diodes to handle more power [22]. The second configuration shown in Figure 1(b) combines the rectified DC output voltage of all antennas but reduces the efficiency of the system [23]. Figure 1(c) shows a hybrid configuration of an array rectenna in which both the RF combination of incoming signals and the DC combination of rectified signals are shown for a greater voltage output.

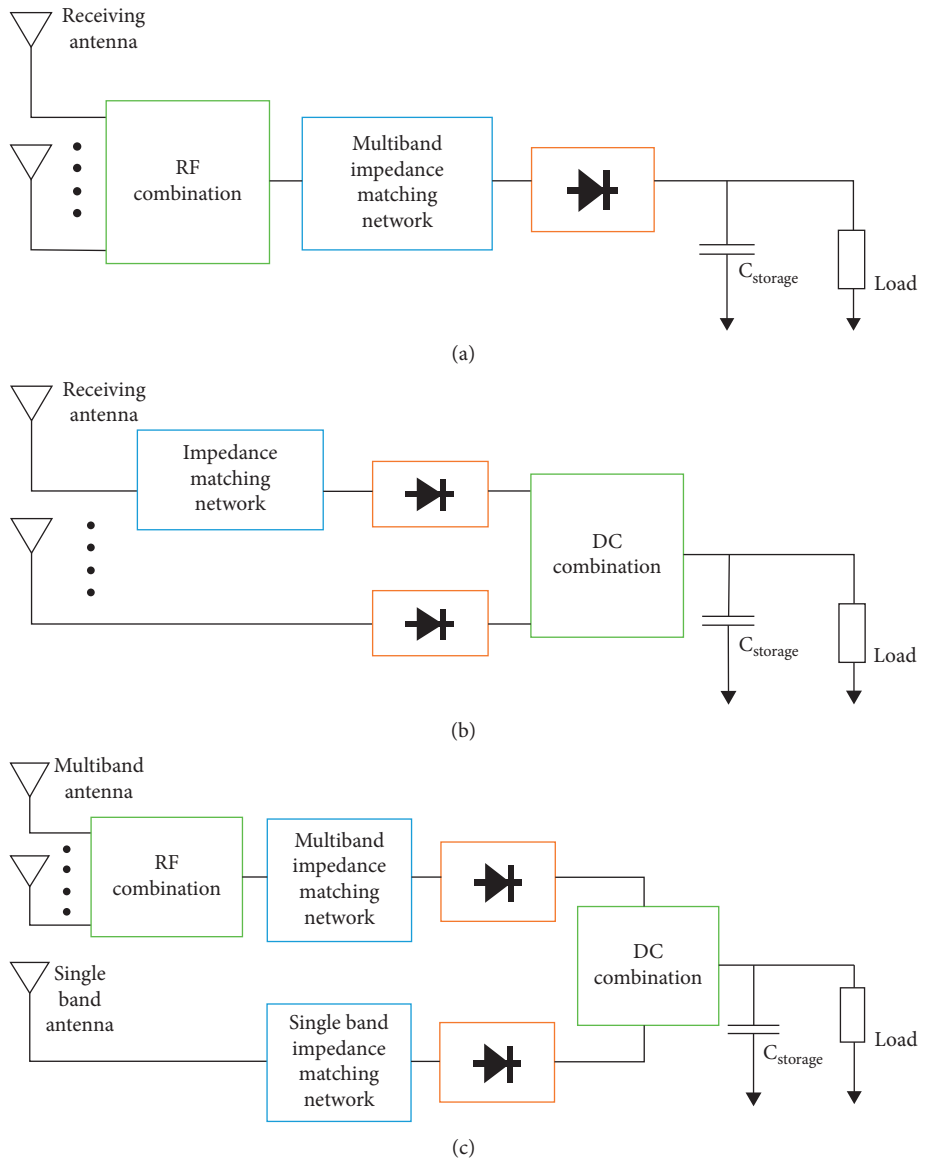

FIGURE 1: Rectenna array topologies. (a) Multiple antennas with RF combination and single multiband rectifier. (b) Multiple antennas with separate rectifiers and DC combination. (c) Proposed hybrid topology.

The proposed rectenna is modelled as a cube with multiband cross-dipole antennas on four sides and FM monopole antenna acting as the hanging structure at the top. The cubic shape is chosen to enable housing of multiple printed circuit boards (PCBs) in a compact form factor as well as to scavenge available energy from all directions. Based on the cubic rectenna design, a hybrid array topology that utilizes both RF and DC combinations depicted in Figure 1(c) is used. The energy received by the multiband antennas is combined and transferred to the matched rectifier housed within the cube. Separate rectifiers are used for multiband and FM antennas and the DC output of both is recombined. Figure 2 shows the internal components of the cubic rectenna. The hybrid array topology from Figure 1(c) was selected in order to demonstrate the proof of concept design of a rectenna system that utilizes multiple signal combinations and covers a wide frequency spectrum.

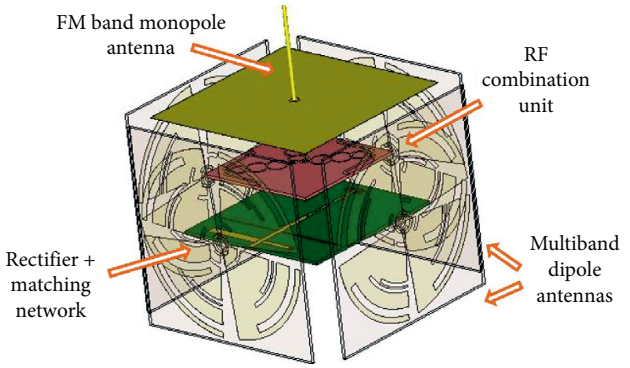

FIGURE 2: 3D cube rectenna structure.

In order to achieve higher DC power at the output, a novel concept of an RF energy harvesting (EH) tree is proposed. The proposed cubic rectenna module will act as

the integral unit of the EH tree. The larger part of the rectenna, i.e., the FM antenna, can be easily integrated with the supposed branches of the tree while the multiband antennas will act as leaves (see Figure 3). The harvested voltage can be transferred to the centre of the tree through the FM antenna. The design also introduces two levels of DC combination: (1) the combination of DC power from FM and multiband rectennas (as shown in Figure 1(c)) and (2) the combination of DC power from multiple rectenna modules on the tree structure. This concept of energy harvesting can be extended to include any frequency including the AM band at the lower end and higher frequency bands. The FM, AM, and broadcasting bands are potential energy sources, but their use is limited due to the large antenna size at these frequencies. The tree structure provides an ideal way to make use of such large antennas into an energy harvesting system. The design approach is similar to existing prototypes of EH trees, which utilize solar and wind energy as a way towards green and sustainable power sources [24, 25]. The design emulates the process of photosynthesis, which can be seen as nature's energy harvesting mechanism whereby fuel is created and transferred from the leaves to the rest of the tree. The goal of the system is to harvest maximum amount of energy from the environment while the structure itself should be blended in the topography appearing practically invisible.

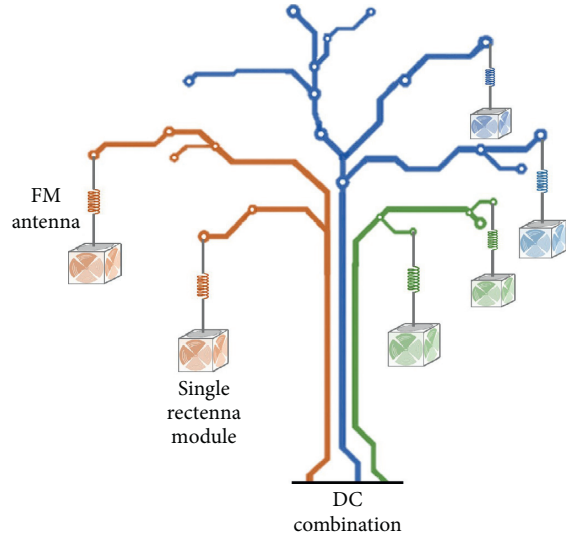

Figure 3: Conceptual diagram of energy harvesting system.

3. Ambient RF Energy Survey

Analysis of ambient energy density in an area is a complex task as it depends on distance from RF sources, their transmit powers, quantity, and distribution of these sources as well as terrain. Accurate estimation of power density requires either exact path loss models acquired from experimental measurements or analytical modelling. This is why no general solution of ambient energy density calculation exists. Therefore, power measurements in multiple locations of the desired area and subsequent averaging of the results are the most viable solution and have been adopted in this work. The ambient RF field measurements conducted in this work are a continuation of the tests performed in [26].

3.1. Methodology and Test Setup. The ambient RF measurements were carried out at multiple locations at the university campus, which lies in a semiurban environment. Figure 4 shows the general testing setup whereas the floor plans of the indoor and outdoor measurement sites, measurement locations and distribution of RF sources like nearest communication towers, and Wi-Fi routers are shown in Figure 5. The indoor measurement points were chosen to be in different parts of the building like labs and lounge. Outdoor measurement was carried out at different points in the grounds surrounding the campus as well as on the campus terrace. Together, all the measurement points were located within a radius of nearly 1 km. Although a number of cellular and broadcasting sources were present in the broader vicinity, the closest cellular tower lies about 0.3 km away and the closest FM source is nearly 6.2 km away

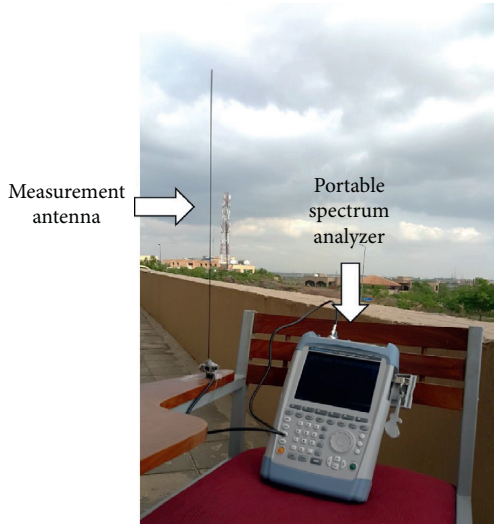

Figure 4: Measurement setup.

from the measurement area as mapped out in Figure 5. Multiple Wi-Fi sources are also present inside the building. The equipment used for ambient energy measurement included a portable spectrum analyzer and a set of broadband omnidirectional whip antennas with a frequency range of few MHz to 2.7 GHz were used. With measured data for each location, the average power density for each frequency band was calculated. The antenna power factor and cable losses were deembedded from the measurements. Multiple measurement trials were conducted spreading over several days to ensure data repeatability. Since ambient RF power is not constant and changes with time of day and presence of active devices in vicinity, the standard deviation of the collected data from the mean is also calculated.

The results of the RF field survey are shown in Figure 6, whereas Table 1 summarizes the indoor vs. outdoor available power levels from different sources along with standard frequency ranges. The uplink and downlink bands are

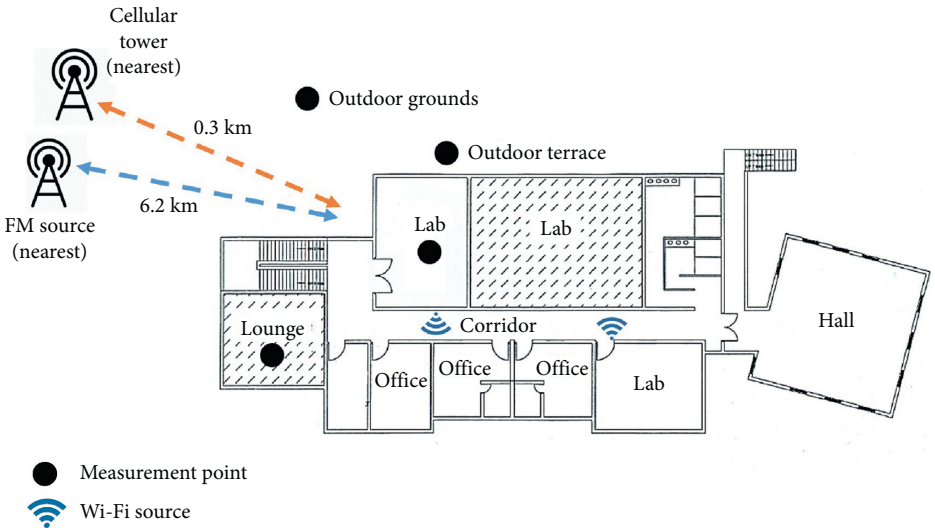

Figure 5: Floor plans of testing site with nearest energy harvesting sources (distances are not realistic and have been scaled down to fit image).

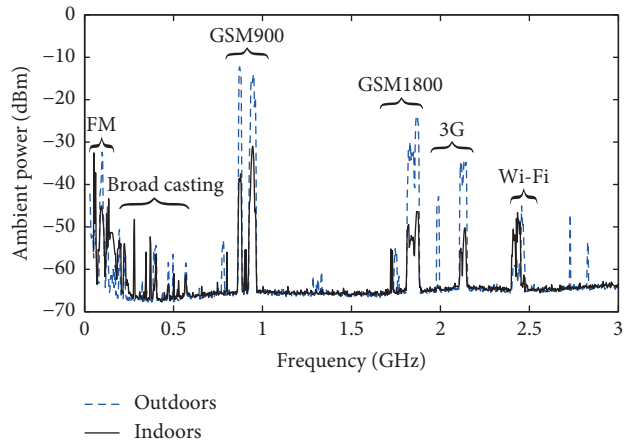

Figure 6: Peak ambient power vs. frequency in a semiurban environment.

denoted by UTx and DTx, respectively, and the power available in the environment is found by

$$W_i = A_e P_T, \quad (1)$$

where W_i and P_T are the power density of incident wave and the power delivered to the spectrum analyzer, respectively, and A_e is the effective antenna aperture. The peak available power values are recorded between −60 dBm and −10 dBm with average ambient values between −15 and −30 dBm.

3.2. Results and Discussion. From the RF survey, FM broadcasting, GSM900, GSM1800, 3G, and Wi-Fi were identified as potentially useful ambient RF energy sources. GSM900 shows maximum peak power whereas FM and broadcasting sources appear to be heavily dependent on line-of-sight and Wi-Fi is very dependent on user traffic. GSM900 shows higher power level in the uplink while GSM1800 and 3G show greater power in the downlink. The outdoor measurements show higher levels of GSM900 and broadcasting signals due to close proximity to a base station and a near line-of-sight from a TV transmitter. Mobile communication sources show much less power indoors whereas Wi-Fi sources show relatively constant power in both indoor and outdoor measurements as there are numerous sources present around campus. The energy available in cellular communication bands and the Wi-Fi band shows the greatest amount of deviation depending upon time. This can be attributed to dynamic user traffic. FM and broadcasting energy sources show comparatively lower deviation.

Wi-Fi sources have low transmit power and are usually found indoors. This makes them more suited for energy harvesting for devices used inside homes and buildings like wearable electronics and domestic sensing devices. On the other hand, mobile communication and broadcasting sources can be used to power sensors in outdoor environment due to higher transmit power of base stations and their omnipresence across the globe. The results also confirm the need of multiband antennas to meet practical requirements.

On the basis of the above analysis, the FM, GSM900, GSM1800, and Wi-Fi bands have been exploited for the proposed rectenna design. 3G band shows promising ambient energy availability, which will be incorporated in our rectenna as a future work.

4. Antenna Design

4.1. Multiband Dual LP Antenna. To harvest energy from the GSM900, GSM1800, and 2.4 GHz Wi-Fi band, a multiband antenna consisting of a modified cross-dipole antenna is designed. The cross-dipole antenna is selected based on its wide bandwidth, bidirectional radiation pattern, and dual linearly polarized (LP) characteristics. The antenna is made on an FR4 substrate with relative permittivity of 4.3 and a thickness of 1.6 mm. The size of the PCB is selected as $100 \times 100\ \text{mm}^2$, which is $0.3\lambda_0 \times 0.3\lambda_0$ at the lowest

Table 1: Peak ambient power level survey.

Frequency band/range (MHz)	Peak available power/power density				Standard deviation (σ)
	Indoor		Outdoor		
	P_T (dBm)	W_i (μW/m^2)	P_T (dBm)	W_i (μW/m^2)	
FM (88–108)	−45	0.0095	−29.56	0.332	2.098
Broadcasting (150–600)	−54	0.00497	−27.58	2.18	5.659
GSM900 UTx (860–915)	−28.41	34.5	−8.991	300	18.48
DTx (925–960)	−37.5	5.91	−19.87	290	11.16
GSM1800 UTx (1710–1785)	−60.1	0.091	−43.3	4.37	7.385
DTx (1805–1880)	−45.4	3.15	−40.89	8.9	15.23
3G UTx (1920–1980)	−51.547	0.82	−31.07	91.9	10.26
DTx (2110–2140)	−49	1.7	−21.45	100	8.592
Wi-Fi (2390–2490)	−42.4	10.7	−47.75	3.15	10.43

operating frequency of 900 MHz. The radius and angle of the bowtie shape are selected as 50 mm and 80°, respectively. Two pairs of cross dipoles are orthogonally printed on each side of the PCB. The antenna is probe fed by a 50 Ω coaxial cable. The inner conductor of the coaxial cable is fed to the top side metal and the outer conductor is connected to the bottom side. The dipole antenna has a balanced topology and typically requires a balun to connect to a coaxial cable. However, in this case, the bandwidth is limited and the antenna is being matched to a 50 Ω impedance so omitting a balun structure does not affect the overall antenna performance. This has also been done to maintain the simplicity and ease of integration of the cubic rectenna structure. The same feeding structure has been employed in a number of other antenna designs without the use of a balun in cross-dipole to coaxial transition ([10, 27–29]).

A simplified cross-dipole is designed for an arbitrary frequency lying between 900 MHz and 2.4 GHz. The proposed cross-dipole resonates at 1.6 GHz with a wide bandwidth of nearly 800 MHz. In order to cover more bands at higher frequencies (up to 2.4 GHz), the cross-dipole is modified by adding a number of slots of different dimensions. Figure 7 shows the modified dipole arm with arbitrary number of slots. This converts each arm of the cross-dipole into a number of bent dipoles defined by a circular part $(L_n + W_n \sec(\theta_n))$ and a radial edge (R_n) where θ_n is the angle of the dipole arm. The total length of each bent dipole arm can be estimated as

$$L_n + W_n \sec(\theta_t) + R_n = \frac{\lambda_n}{4}, \quad (2)$$

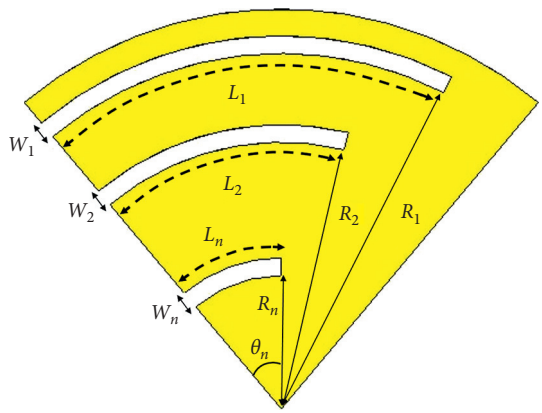

Figure 7: Slotted dipole arm.

where θ_t is the angle of the cross dipole and λ_n is the wavelength of the n_{th} frequency obtained using suspended strip-line model [30]. The parameter L_n is the arc length and can be calculated by $L_n = R_n\theta_n$. The overall bandwidth can be increased by increasing the width (centre angle) of the cross-dipole, whereas the bandwidth of each individual band can be fine-tuned by adjusting the slot width.

The design iterations of the antenna are shown in Figure 8. Table 2 shows the optimized dimensions of slots added to dipole arm to make the antenna resonate at specific frequencies. The simulated S_{11} of the multiple stages of the antenna design is shown in Figure 9. It can be seen that increasing the number of slots introduces a multiband response; however, matching of the antenna is degraded. To

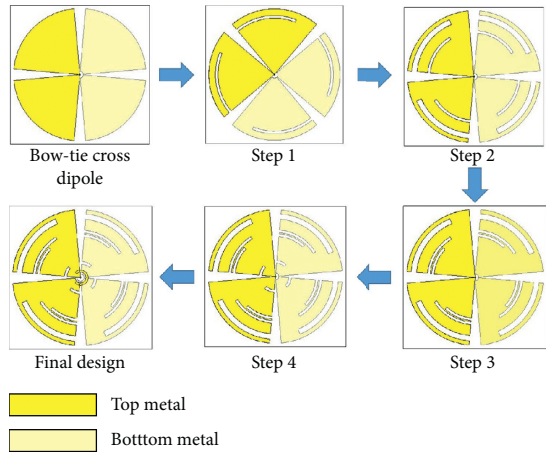

Figure 8: Antenna design iterations, introduction of slots for multiband response and vacant quarter ring to improve matching.

Table 2: Parameters of the proposed slotted cross-dipole antenna.

Resonant operating frequency (MHz)	R_n (mm)	W_n (mm)	θ_n (deg)	$L_n = R_n\theta_n$ (mm)	$L_n + W_n\sec(\theta) + R_n$ (mm)	$\lambda_n/4$ (mm)
875	43	4	65	48.78	85.75	85.71
1730	33	2	50	28.79	43.68	41.67
2100	30	2	45	23.56	35.44	35.71
2400	15	2	40	10.47	28.08	31.25
Antenna dimensions						
	W_a (mm)	R_a (mm)	θ_a (deg)	R_r (mm)	W_r (mm)	
	100	50	80	4	1.6	

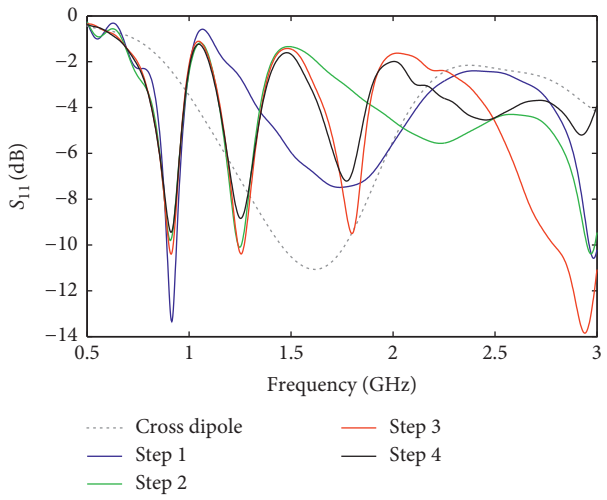

Figure 9: The simulated S_{11} of the proposed antenna versus frequency for different design steps.

overcome this a printed vacant quarter ring is added to the structure.

The vacant ring is significantly able to improve the antenna performance. It helps in the matching of the antenna in its operating bands. The matching performance is greatly dependent on the dimensions of this feeding ring. To achieve a good matching at all frequencies of interest the width and radius of the ring are optimized using parametric analysis to 4 mm and 1.6 mm, respectively. Figure 10 shows the final antenna design along with its dimensions. Figure 11 shows the simulated and measured S_{11} of the proposed multiband antenna. Addition of the vacant ring improves the matching performance of the antenna, which covers the following bands: GSM900 (720 MHz to 940 MHz), GSM-1800 (1650 MHz to 1760 MHz), and Wi-Fi (2.334 GHz to 2.43 GHz). The individual multiband antenna has a peak gain of 1.6, 2.4, and 5.3 dBi at 0.9, 1.73, and 2.4 GHz, respectively.

The antenna exhibits dual linear polarization due to the orthogonal arrangement of the dipoles. This allows the antenna to receive energy from diversely polarized sources. Figure 12 shows the surface current distribution at the frequencies of interest. It can be seen that the current flows through the longest bent dipole at lowest frequency and vice versa. Figure 13 shows the 2D radiation patterns of the individual antenna while Figure 14 shows the simulated 3D radiation patterns. The radiation patterns are of the standalone antenna. The patterns are similar in the lower frequency band. The difference arises at the higher frequency and is mainly attributed to the measurement equipment. Also, higher order modes are excited at the higher frequency resulting in more lobes in the radiation patterns of the antenna.

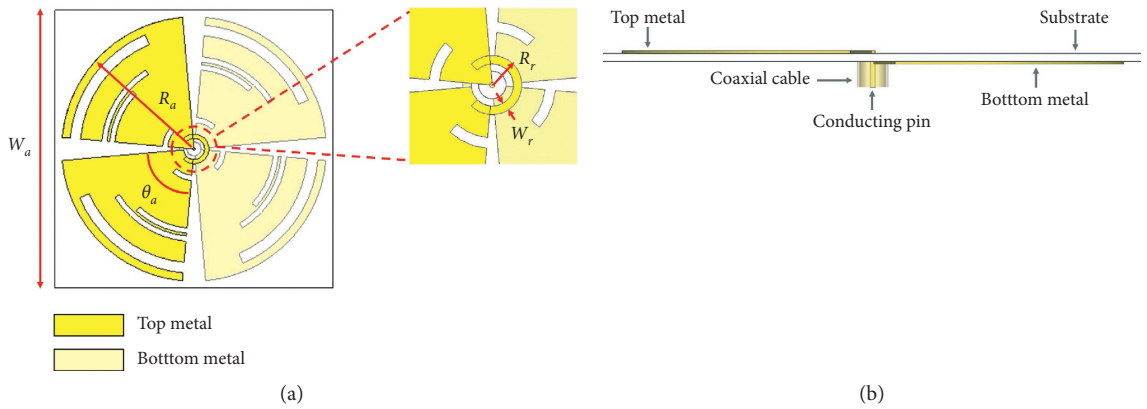

Figure 10: Proposed antenna design. (a) Front view. (b) Side view.

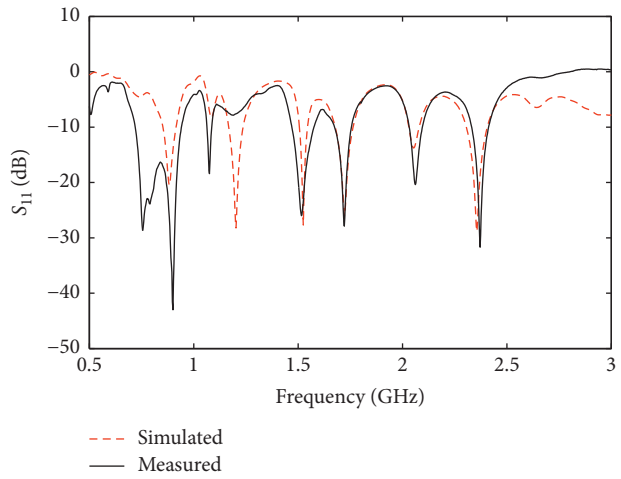

Figure 11: Simulated and measured S_{11} of the proposed antenna versus frequency.

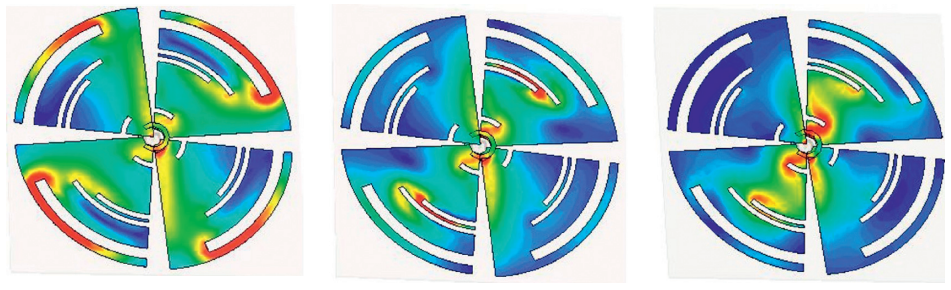

Figure 12: Current distribution of the antenna. (a) 875 MHz. (b) 1730 MHz. (c) 2400 MHz.

4.2. FM Band Antenna Design. An inductively loaded monopole antenna at 98 MHz is designed for energy harvesting in FM band. In order to minimize the size of otherwise large FM antenna an inductively loaded coil is added to the monopole reducing the antenna size and improving performance. The loading coil placement on the monopole rather than the feed point also provides greater radiation efficiency. The exact location of loading point is typically based on bandwidth and size requirement. Loading nearer to the feed (at 33% or 66%) provides better radiation performance. However, loading near the end results in antenna size reduction [31]. The antenna has a $10 \times 10\,\text{cm}^2$ reflector at the bottom to enhance gain. Figure 15 shows the design of the proposed antenna along with dimensions.

The loading point for the monopole can be denoted as the ratio of lower monopole length and the total length of the antenna.

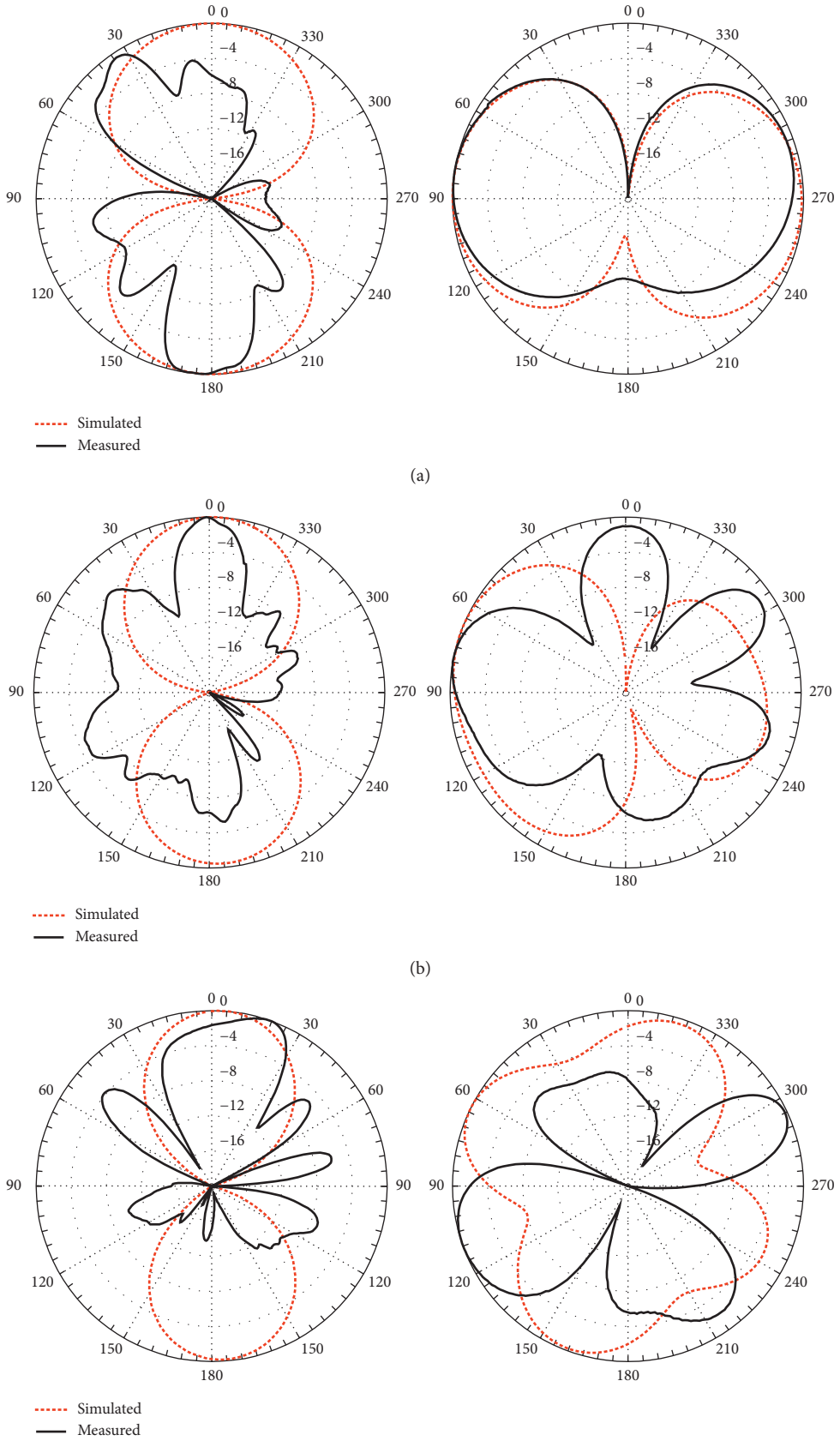

Figure 13: Comparison between the simulated and measured 2D radiation patterns for XZ plane (left) and XY plane (right) at (a) 900, (b) 1730, and (c) 2400 MHz.

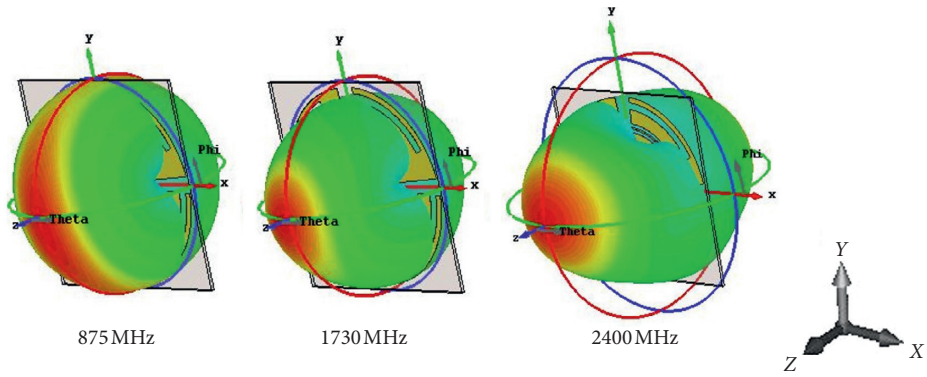

Figure 14: 3D radiation patterns of antenna.

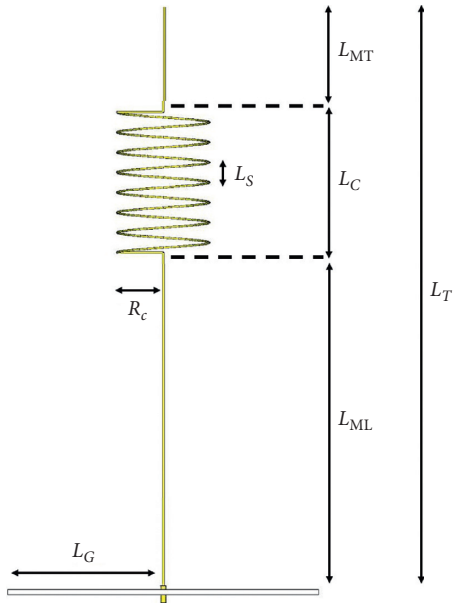

Figure 15: Side view of proposed loaded monopole antenna ($L_T = 55$, $L_{ML} = 37$, $L_{MT} = 11$, $L_C = 7$, $L_S = 1$, $L_G = 5$, $R_C = 2$).

$$m = \frac{L_{ML}}{L_T}. \tag{3}$$

The required resonance is achieved at $m = 0.67$ with the size reduced to 55 cm ($0.18\lambda_0$) in case of loading as opposed to nearly 160 cm when no loading coil is used. Figure 16 shows the simulated and measured S_{11} while gain of 1.76 dBi is obtained from the antenna.

RF combination of the multiband antennas has been done using a 1×4 Wilkinson power combiner covering a frequency range of 0.5 to 3 GHz. The 4-way combiner has been designed using three 2-way combiners. Each combiner consists of three semi-circular transmission line sections of different widths to give a wideband response at the frequency range of interest. The transmission line impedances and resistor values for each section are shown in Table 3. It is fabricated on FR4 substrate with thickness of 1.6 mm and relative permittivity of 4.3. The insertion loss, isolation, return loss, and phase of the combiner at input and output ports are shown in Figure 17, where port 1

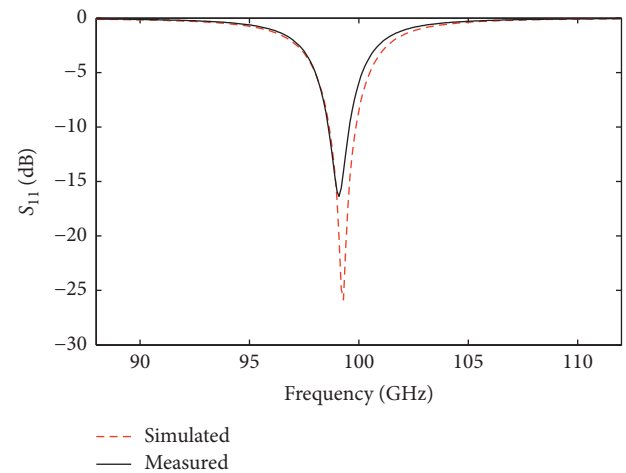

Figure 16: Simulated and measured S_{11} of loaded monopole antenna.

Table 3: Power combiner parameters.

Parameter	Z_1	Z_2	Z_3	R_1	R_2	R_3
Value (Ω)	93.33	78.16	64.18	120	220	470

is the output port with combined RF power and ports 2 to 5 are input ports. The ports of the combiner are designed in an orthogonal arrangement so that they can be easily inserted in the energy harvesting cube with connections to four antennas on the side (Figures 18(a) and 18(b)). The drawback of the proposed power combiner is the degradation in output voltage of the rectenna due to phase differences in incoming signals. In an ambient environment, the power level and phase of available signals are completely unpredictable and random in nature, thus making the design of an efficient power combiner considerably difficult. The rectenna performance in the worst case scenario (i.e., completely out of phase incoming signals) was simulated and the output voltage was noted to be lower than that in other cases. However, in real scenarios the ambient power is rarely completely out of phase and shows slight phase differences. In this work, the proposed combiner is utilized due to its superior performance over other combiner designs, simplicity of design, and ease of

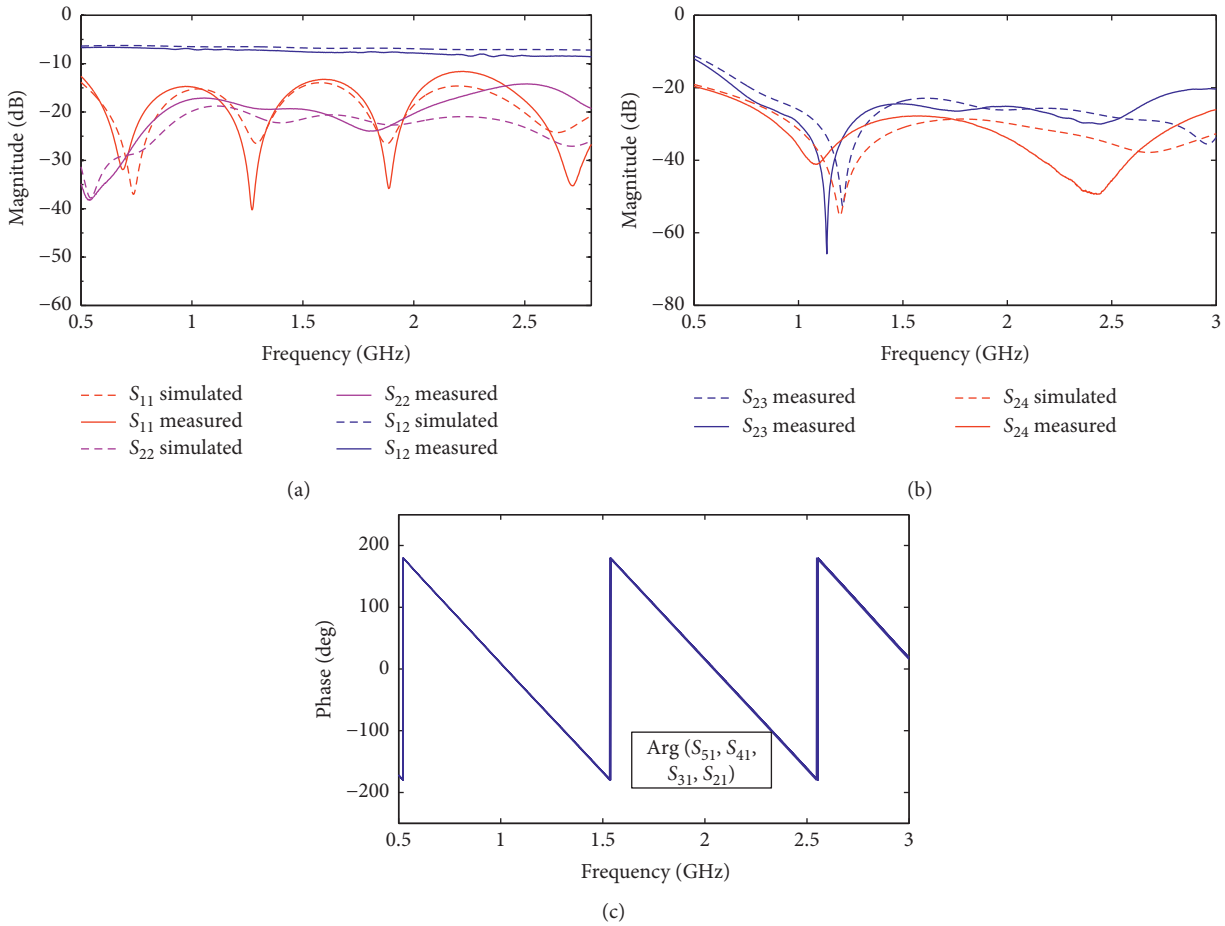

FIGURE 17: Simulated and measured S parameters of the power combiner. (a) Insertion loss and return loss at input and output ports. (b) Isolation between adjacent and opposite input ports. (c) Transmission phase.

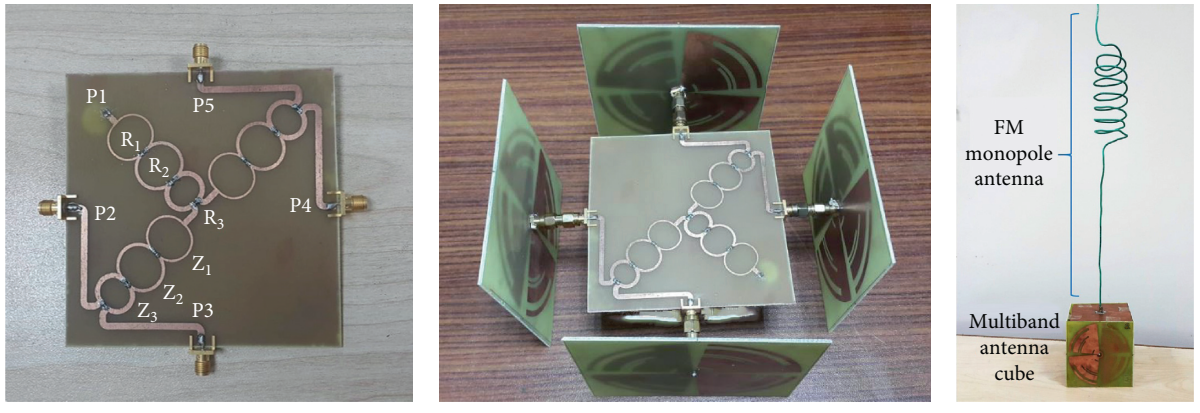

FIGURE 18: Integration of antennas to form one harvesting node. (a) Power combiner. (b) Combiner with multiband antennas. (c) Proposed 3D rectenna module.

integration with the antennas and rectifier. The multiband and FM antennas are integrated to form a 3D harvesting node of the proposed harvesting system. The end product is a $10 \times 10 \times 10\,\text{cm}^3$ cube with a 55 cm hanging FM antenna on top. It can also be seen from Figure 18(c) that the top side of the cube acts as a reflector of the FM antenna. This cubic arrangement of multiband antennas helps increase individual antenna gains to 2.34, 2.5, and 6.3 dBi at 0.9, 1.8, and 2.4 GHz, respectively, and makes the rectenna virtually omnidirectional.

A number of structures (adjacent antennas, opposing antennas, triangular, and cubic arrangement) were analysed for the final form of the energy harvesting node. The cubic structure was selected due to better gain and radiation characteristics and ease of integration of inner components. The analysis of radiation characteristics of the antennas in the vicinity of each other has also been done. At 0.9 and 1.73 GHz the energy harvesting cube shows an overall gain increase from 1.6 to 3 dBi at 0.9 GHz and from 2.4 to 4.72 dBi at 1.73 GHz, respectively. Similarly, at 2.4 GHz the gain marginally decreases from 5.3 to 4.9 dBi. Due to the size and placement of the antennas the overall gain and efficiency do not alter much after the cubic structure is employed. The obtained radiation efficiency of the antenna system is around 90%, 80%, and 70% in GSM900, GSM1800, and Wi-Fi bands, respectively. The choice of antenna or type of antenna arrangement does not have a significant effect on the conversion efficiency as it is measured using the RF power input to the rectifier. The antenna arrangement only determines the level of this input RF power.

5. Rectifier Design

The three commonly used rectifier topologies for rectenna include single series diode, voltage doubler, and the Greinacher rectifiers. A single diode is preferred when input power levels are very low, whereas the Greinacher rectifier is used for applications involving higher power handling. The ambient power levels range from low to medium intensity. Therefore, the voltage doubler topology is chosen due its high power handling capability, low input voltage requirement (depending on diode), and doubled output DC voltage. The voltage doubler has been constructed using Skyworks SMS7630 diodes and 100 nF Murata GRM188 series capacitors. The SMS7630 has a low threshold voltage and exhibits high sensitivity at low input power levels, thus making it ideal for power harvesting applications. A load resistance of 10 kΩ is chosen as it represents the typical resistance value of IoT sensors. The rectifier circuit is simulated in an electronic design automation software, namely, Advanced Design System (ADS), to accurately model the parasitics arising due to the capacitors. Figure 19 shows the simulated complex input impedance of the voltage doubler for multiple power levels (−30 dBm to 0 dBm) at 10 kΩ. It can be observed that the real and imaginary parts of the input impedance decrease with an increase in operating frequency and increase with an increase in the input power levels.

6. Matching Network Design

The multiband impedance matching network is required between antennas and rectifier circuit for four frequency bands (0.098, 0.9, 1.8, and 2.4 GHz) and is designed through a combination of a Triband matching network for 0.9, 1.8, and 2.4 GHz and a separate matching circuit for 98 MHz.

6.1. Triband Matching Network. The triband matching network is required to match the complex rectifier impedance at 0.9, 1.8, and 2.4 GHz to 50 Ω antenna resistance. It is a combination of a Dual Band Impedance Transformer (DBIT) and a Dual-to-Triband Impedance Transformer (DTBT) as shown in Figure 20 [32]. The former transforms the Frequency Dependent Complex Load (FDCL) impedance at the first two frequency bands of 0.9 GHz and 1.8 GHz to 50 Ω while the DTBT transforms the complex DBIT input impedance at the third frequency band of 2.4 GHz.

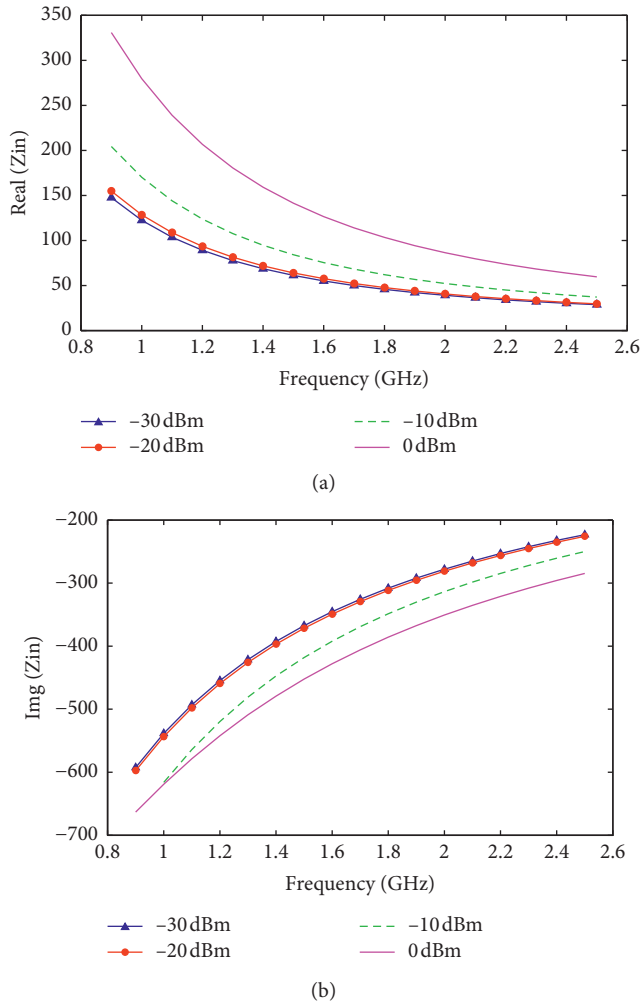

Figure 19: Input impedance of the voltage doubler rectifier versus frequency and input power levels for 10 kΩ load. (a) Real part. (b) Imaginary part.

6.1.1. Dual Band Impedance Matching Network. With an aim to derive a closed form solution, the schematic of DBIT is shown in Figure 21 where $Z_{L1} = R_a + jX_a$ and $Z_{L2} = R_b + jX_b$. Stage I transforms the complex load impedance at f_1 and f_2 to pair of complex conjugate impedances "Z_{L2}" such that $Z_{L2} \mid f_1 = (Z_{L2} \mid f_2)^*$.

The two series transmission lines of stage II transform Z_{L2} impedance to Z_0 resistance at the first two frequency bands. The characteristic impedance and length of stage I transmission line are obtained using the following set of equations [21]:

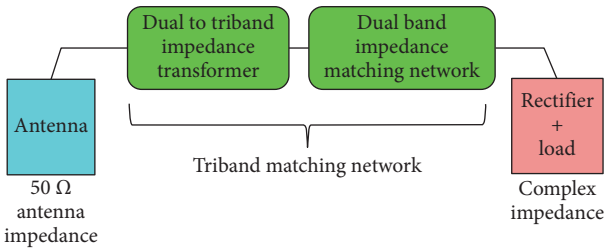

Figure 20: Block diagram of the Triband Impedance Matching Network (TIMN).

$$Z_s = \sqrt{R_a R_b + X_a X_b + \frac{X_a + X_b}{R_b - R_a}\left(R_a X_b - R_b X_a\right)},$$
$$l_3 = \frac{n\prod + \arctan\left(\left(Z_3\left(R_a - R_b\right)\right)/\left(R_a X_b - R_b X_a\right)\right)}{(m+1)\beta_a}. \quad (4)$$

The input impedance of stage II is found using the following transmission line equations:

$$Z_0 = Z_{\text{in}} = Z_1 \frac{Z_{L1} + jZ_1 \tan\left(\beta_a l_1\right)}{Z_1 + jZ_{L1} \tan\left(\beta_a l_1\right)}, \quad (5)$$

$$Z_{L1} = Z_2 \frac{Z_{L2} + jZ_2 \tan\left(\beta_b l_2\right)}{Z_2 + jZ_{L2}@f_3 \tan\left(\beta_b l_2\right)}, \quad (6)$$

whereas the TL parameters for stage II are obtained using the following equations:

$$l = l_1 = l_2 = \frac{\prod}{\beta_a + \beta_b}, \quad (7)$$

$$Z_1^4 + bZ_1^3 + cZ_1^2 + dZ_1 + e = 0, \quad (8)$$

where

$$b = \frac{2aR_0X_{L2}}{R_0 - RL2},$$
$$c = \frac{R_0R_{L2}\left(X_{L2}^2 - \left(R_0 - R_{L2}\right)^2\right) - X_{L2}^2R_0^2\left(1 + a^2\right)^2}{a^2R_{L2}\left(R_{L2} - R_0\right)},$$
$$d = \frac{2aR_0^3X_{L2}}{RL2 - R_0}, \quad (9)$$
$$e = \frac{R_0^3\left(R_{L2}^2 + X_{L2}^2 - R_0R_{L2}\right)}{R_0 - R_{L2}}.$$

From (8), the value of Z_1 is obtained, which can be used to find the value of Z_2 using (6). The calculated values of the TL parameters are shown in Figure 22.

6.1.2. Dual-To-Triband Impedance Matching Network. In order to match the third frequency band, the circuit, shown in Figure 23, is used as dual-to-triband impedance transformer (DTBT). It consists of Open-Circuit-Short-Circuit (OCSC) stubs along with a series transmission line having

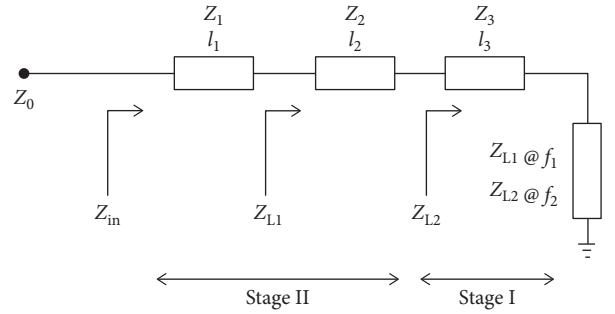

Figure 21: Block diagram of the Dual Band Impedance Transformer (DBIT).

characteristic impedance Z_0, which is the same as the system's characteristic impedance.

The DTBT does not affect the impedance matching that is already achieved at the first two frequency bands through the DBIT. Initially, only the series TL and OCSC-1 stubs are considered. The input impedance of the DBIT at the third frequency band is found using the following equations [33]:

$$Z_{\text{in1}}@f_3 = Z_1 \frac{Z_{L1} + jZ_1 \tan\left(\upsilon\beta_a l_1\right)}{Z_1 + jZ_{L1} \tan\left(\upsilon\beta_a l_1\right)} = G_1 + jB_1, \quad (10)$$

where

$$\upsilon = \frac{f_3}{f_1},$$
$$Z_{L1} = Z_2 \frac{Z_{L2}@f_3 + jZ_2 \tan\left(\beta_b l_2\right)}{Z_2 + jZ_{L2}@f_3 \tan\left(\beta_b l_2\right)}, \quad (11)$$
$$Z_{L2}@f_3 = Z_3 \frac{Z_{L3} + jZ_3 \tan\left(\upsilon\beta_a l_3\right)}{Z_3 + jZ_{L3} \tan\left(\upsilon\beta_a l_3\right)}.$$

The Z_{L3} represents the rectifier's input impedance and β_c is the propagation constant at the third frequency. Since only OCSC-1 is used, therefore, $B_1 = B_2$ and the value of B_3 can be computed using (10) and (12), thus obtaining the values of characteristic impedances of OCSC-1 stubs.

$$B_3 = \frac{\left(1 - Z_0B_2 \tan\upsilon\theta\right)\left(Z_0B_2 + \tan\upsilon\theta\right) - Z_0^2G_1^2 \tan\upsilon\theta}{Z_0\left[\left(1 - Z_0B_2 \tan\upsilon\theta\right)^2 + \left(Z_0G_1 \tan\upsilon\theta\right)^2\right]}. \quad (12)$$

The electrical length "θ" of the series transmission line can be found using (13), which can be used to find the characteristic impedances of the OCSC stubs using (14).

$$\tan\upsilon\theta = \frac{Z_0B_2 \pm \sqrt{\left(Z_0B_2\right)^2 + \left(1 - Z_0G_1\right)\left(Z_0^2B_2^2 + Z_0^2B_2^2\right) - Z_0G_1}}{\left(Z_0^2B_2^2 + Z_0^2B_2^2 - Z_0G_1\right)}, \quad (13)$$

$$Y_a = \frac{B_3}{\tan\upsilon\theta_1 - \tan^2\theta_1 \cot\upsilon\theta_1}, \quad (14)$$

From the calculated value of Z_a, Z_b can be found using (15) and (16).

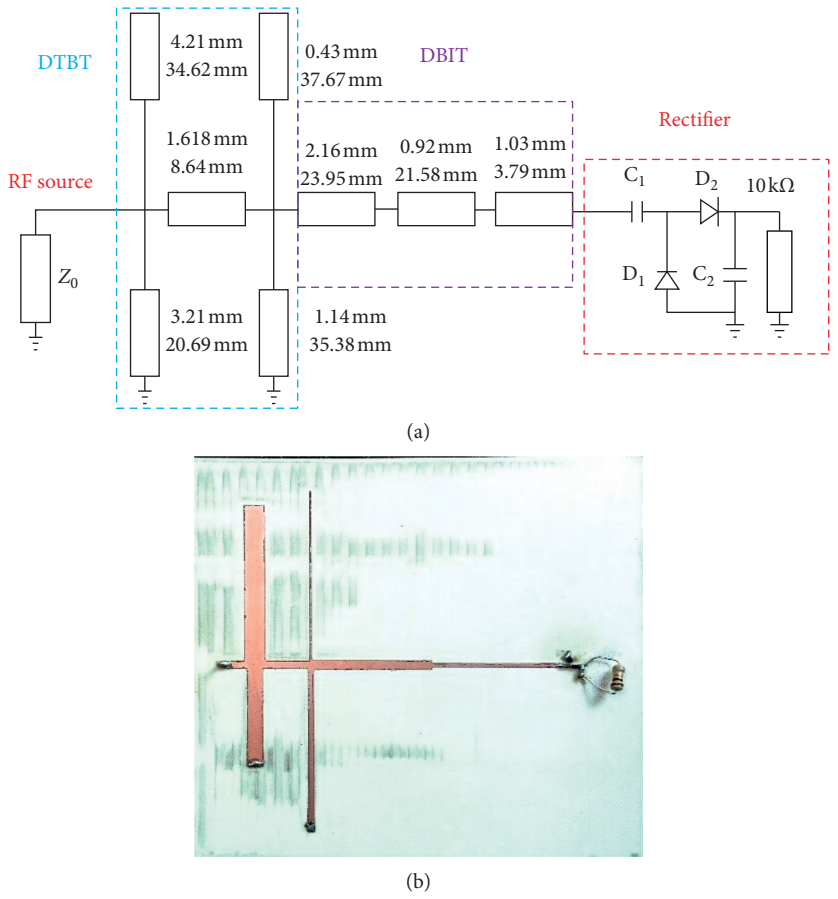

Figure 22: Schematic and prototype of the proposed Triband rectifier (PCB size: $7 \times 7.5\,\text{cm}^2$).

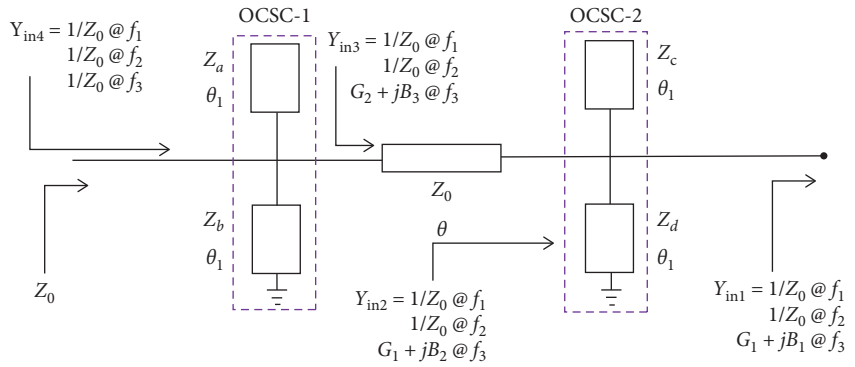

Figure 23: Block diagram of the Dual-to-Triband Impedance Transformer (DTBT).

$$\theta_1 = \frac{(1+s)\prod}{1+r}, \tag{15}$$

$$Z_a = Z_b \tan^2\theta_1. \tag{16}$$

If the calculated characteristic impedances are outside the physically realizable range of 30 Ω to 130 Ω, the design procedure has to be repeated by incorporating OCSC-2 stubs with an assumed of Z_c. The corresponding value of Z_d can be found using (17) as follows:

$$Z_c = Z_d \tan^2\theta_1. \tag{17}$$

The overall design procedure can be summarized as follows:

(1) The transmission line parameters of DBIT are determined by finding the complex load impedances at the first two frequency bands.

(2) The input impedance ($Z_{\text{in1}}@f_3$) of DBIT at the third frequency band is determined using equations or simulations.

(3) This value (i.e., $Z_{in1}@f_3$) is used to calculate the electrical length of the series TL followed by the calculation of electrical length and characteristic impedance values of the OCSC-1 and OCSC-2 stubs.

The calculations are initially carried out for complex load impedances corresponding to 0 dBm input power level obtained from Figure 19 and subsequently the design is optimized in ADS to achieve triband matching at multiple power levels, i.e., −30 to 0 dBm. The schematic and prototype of the matching network along with the parameters are shown in Figure 22. The proposed network uses closed form equations unlike reported works that rely solely on optimization tools. After cosimulation of the network and rectifier, the design is fabricated on a 0.762 mm thick Rogers RO4350B substrate with $\varepsilon_r = 3.48$. The S_{11} is measured using Agilent Technologies E8362B PNA Series Network Analyzer and shown in Figure 24. The proposed triband matching network covers the GSM-900 (870–900 MHz), GSM-1800 (1700–1730 MHz), and Wi-Fi (2360–2390 MHz) band for multiple power levels. The slight shift in the measured results can be attributed to unknown parasitics of the SMD capacitors and diodes. The RF-DC conversion efficiency of the rectifier is calculated using the following equation:

$$\eta_{\text{RF-DC}} = \frac{P_{\text{DC}}}{P_{\text{in}}}, \tag{18}$$

where P_{DC} is the output electrical power while P_{in} is the input RF power to the rectifier. Figure 25 shows the triband rectifier efficiency. The higher efficiency is achieved at 0.9 GHz as compared to 1.8 GHz and 2.4 GHz. This is expected due to increased PCB losses at higher frequencies. It can be seen that the rectifier has the highest efficiency around the input power level of −6 dBm. A maximum efficiency of 77% at 0.9 GHz, 74% at 1.8 GHz, and 54% at 2.4 GHz is obtained at this power level. Although multitone input could not be provided due to equipment limitation, the simulated result for multitone input is shown. It can be observed that the efficiency for multitone input is higher than the individual single tone inputs.

6.2. FM Rectifier Design. The matching network for the FM rectifier is a lumped LC circuit optimized to achieve a −10 dB bandwidth over the FM band with a centre frequency of 98 MHz. The selected values of the inductor and capacitor for the LC circuit are 500 nH and 3.9 pF, respectively.

Figure 26 shows the schematic and prototype of the FM rectifier fabricated on Rogers RO4350B while Figure 27 presents the S_{11} for multiple power levels. Better matching is achieved for higher power with a maximum bandwidth of 10 MHz at −20 dBm.

The simulated and measured efficiency values at 98 MHz are shown in Figure 28 which highlights a good correlation. A maximum efficiency of 80% is achieved at 98 MHz for −6 dBm power level.

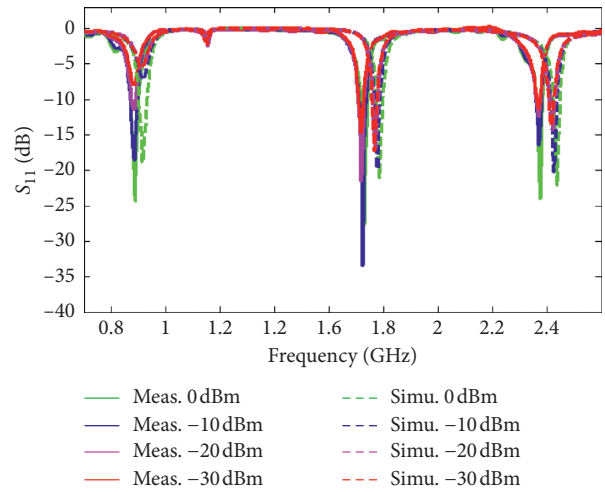

FIGURE 24: Simulated and measured S_{11} of triband rectifier for 10 kΩ load.

6.3. Triband and FM Rectifier Integration. In order to harvest energy simultaneously from four frequency bands, a DC combination of FM rectenna and triband rectenna was designed. Both rectennas use a single rectifier each, making the complete design employ two rectifiers. The RF power of the four triband antennas is combined and fed to one rectifier while the FM antenna is connected to a separate rectifier. The DC combination of both rectifiers is shown in Figure 29(a). Figure 29(b) shows the fabricated prototype of the integrated quad-band rectifier design after DC combination. The substrate used is the same as that for triband rectifier designed earlier. The S_{11} of the integrated multiband rectifier is shown in Figure 30. There is a shift in the FM frequency response as compared to standalone FM rectifier response shown in Figure 27 because of the additional capacitance, which is introduced due to the soldering of matching network lumped components. The big shift in the measured triband response compared to the simulated results can be accounted for by the soldering losses and high frequency losses in the capacitors that were a part of the voltage doubler circuit. Besides this, the parasitic capacitance between the PCB traces has also caused the measured results to shift left. Figure 31 shows the simulated and measured efficiency of the integrated quad-band rectifier at frequencies of interest and multitone input. The DC connection has a negative effect, which can be attributed to the DC combination of two dissimilar rectenna units having different output powers and efficiencies. Due to this, the triband rectenna cannot operate at its optimum efficiency. For this reason there is a reduction of around 10% in the FM efficiency and nearly 40% degradation in the simulated multitone efficiency. A possible solution to increase the total efficiency of the integrated rectifier could be to improve the individual efficiency of the triband rectenna at all the frequency bands so that both the FM and triband rectifiers can achieve optimum operation. This can be done through layout optimization of the rectifier design, which is also a future work of our research group.

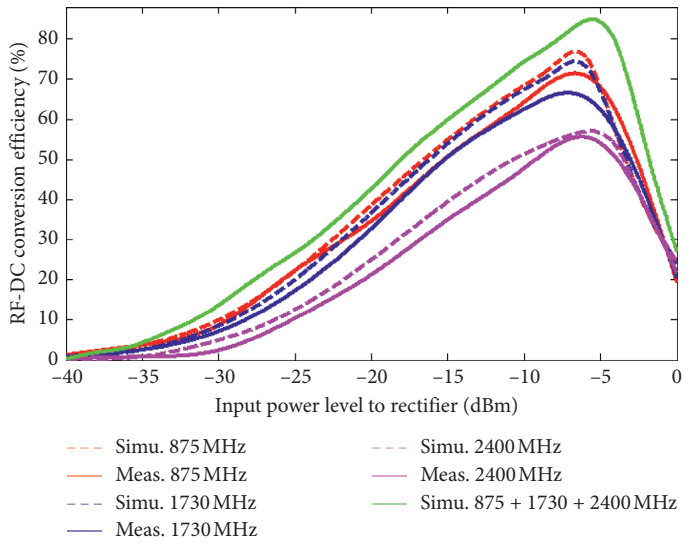

Figure 25: RF-DC conversion efficiency of the triband rectifier for 10 kΩ load.

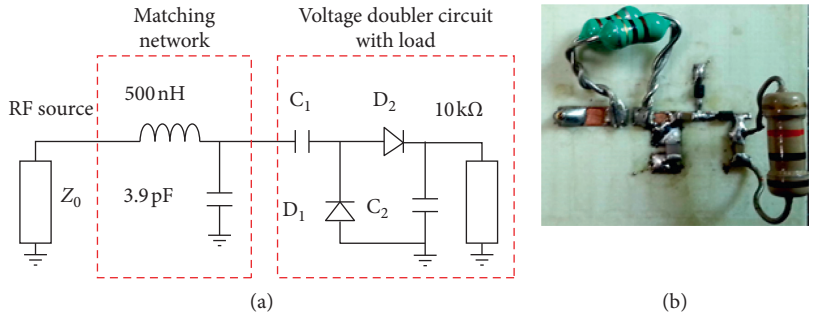

Figure 26: Schematic and prototype of FM rectifier (PCB size: $3.5 \times 2.5\,\text{cm}^2$).

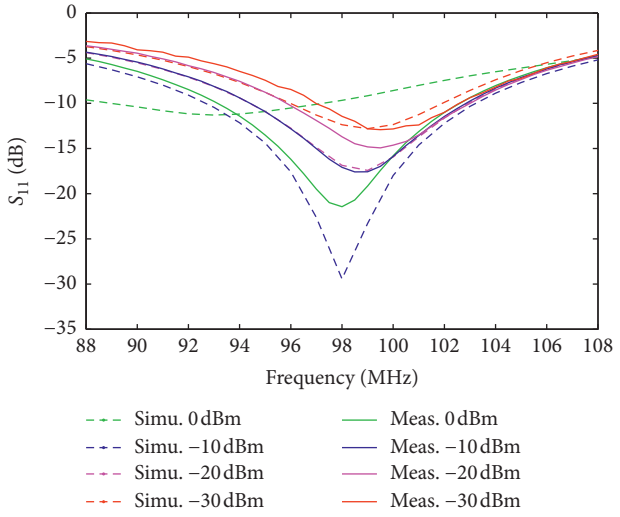

Figure 27: Simulated and measured S_{11} of FM rectifier for 10 kΩ load.

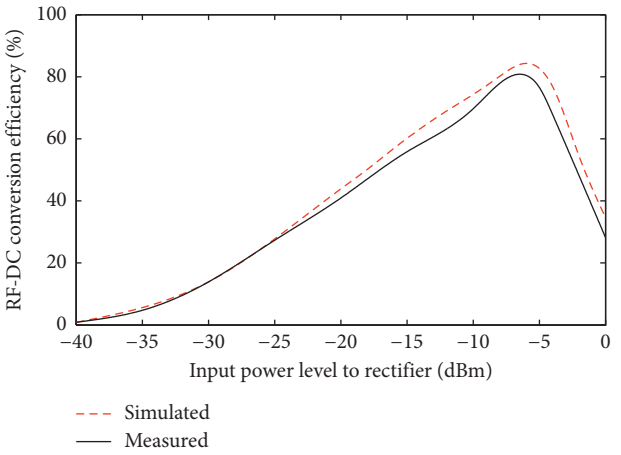

Figure 28: RF-DC conversion efficiency of FM rectifier at 98 MHz for 10 kΩ load.

7. Rectenna Measurements

The integrated rectifier is connected to corresponding antennas (Figure 32). A typical lab at ground level and 24 m^2 area was chosen as the indoor test environment. The outdoor testing was done on an open terrace at a height of 9 m. The rectenna was measured with single multiband antenna as well as with integrated multiband and FM antennas in both indoor and outdoor settings.

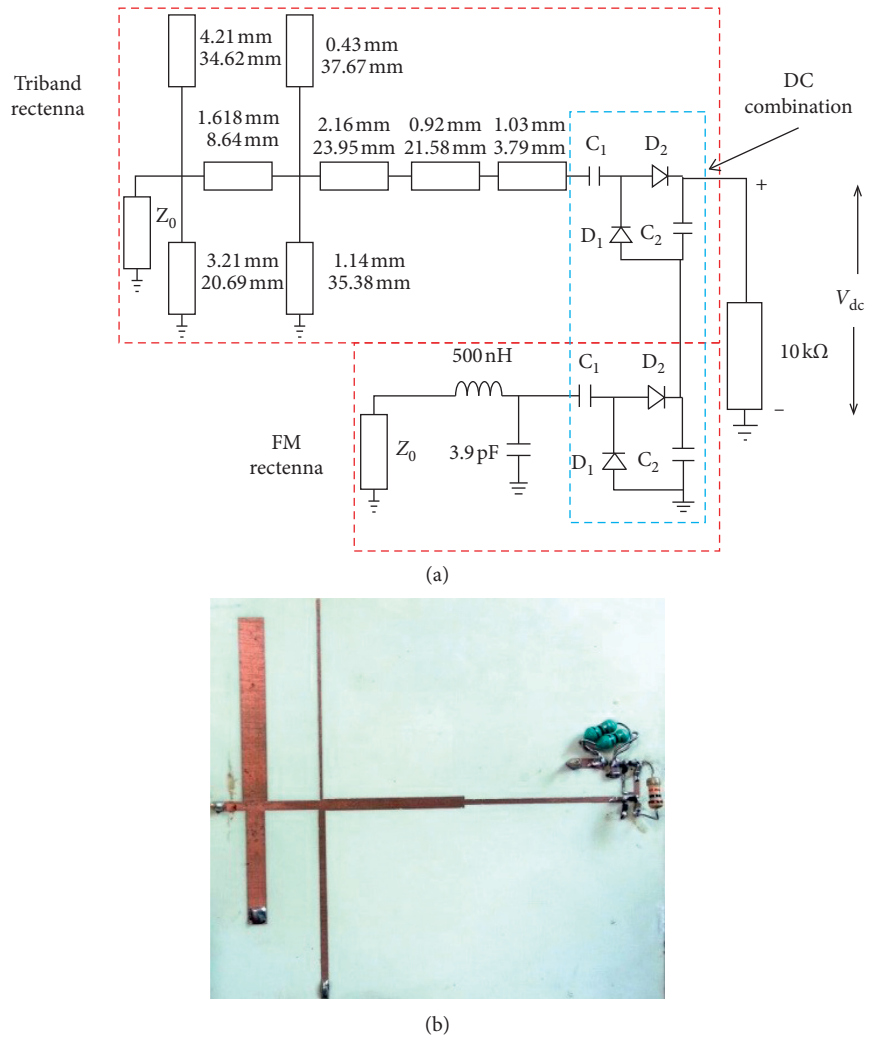

Figure 29: Proposed multiband rectifier. (a) Schematic. (b) Prototype (PCB size: $7 \times 7.5\,\text{cm}^2$).

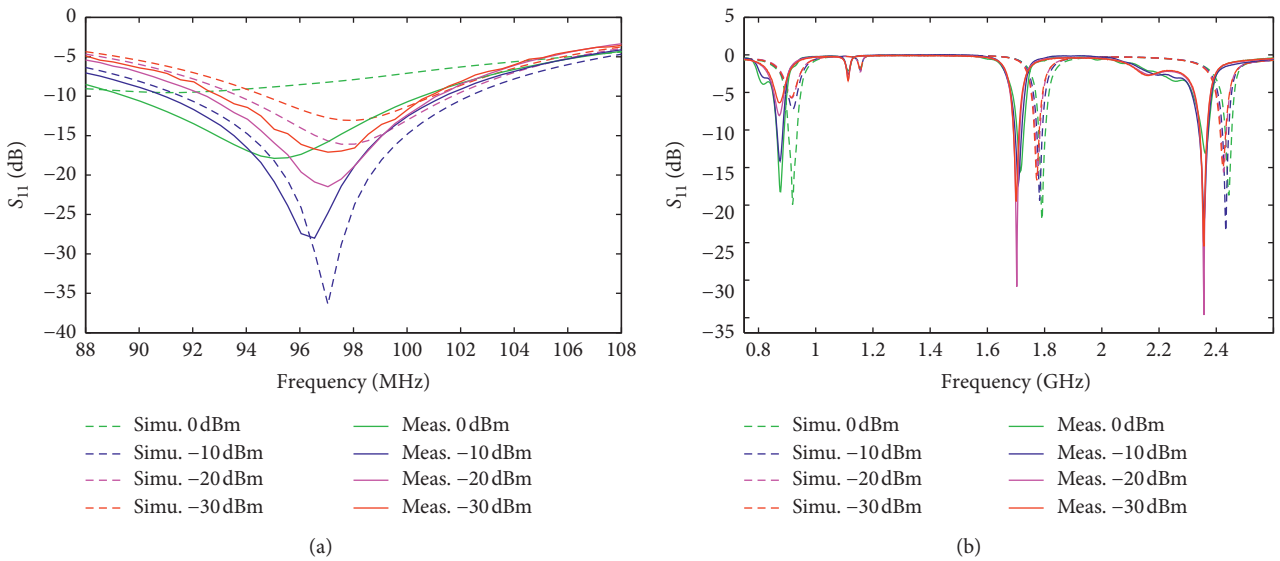

Figure 30: Simulated and measured S_{11} of the integrated multiband rectifier for 10 kΩ load. (a) FM band. (b) Triband.

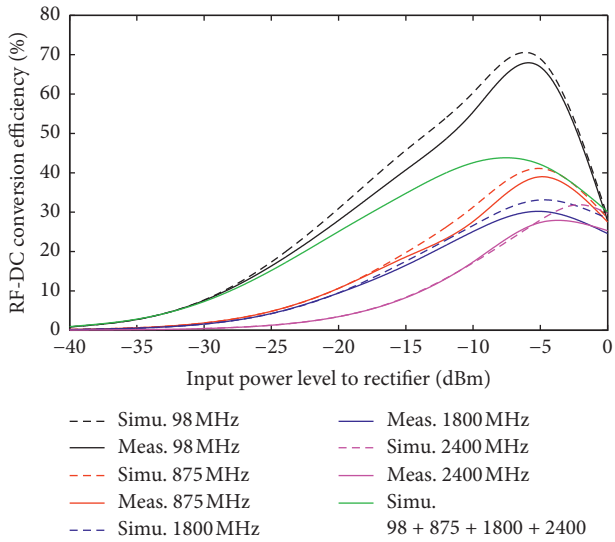

Figure 31: RF-DC conversion efficiency of the integrated multiband rectifier for 10 kΩ load.

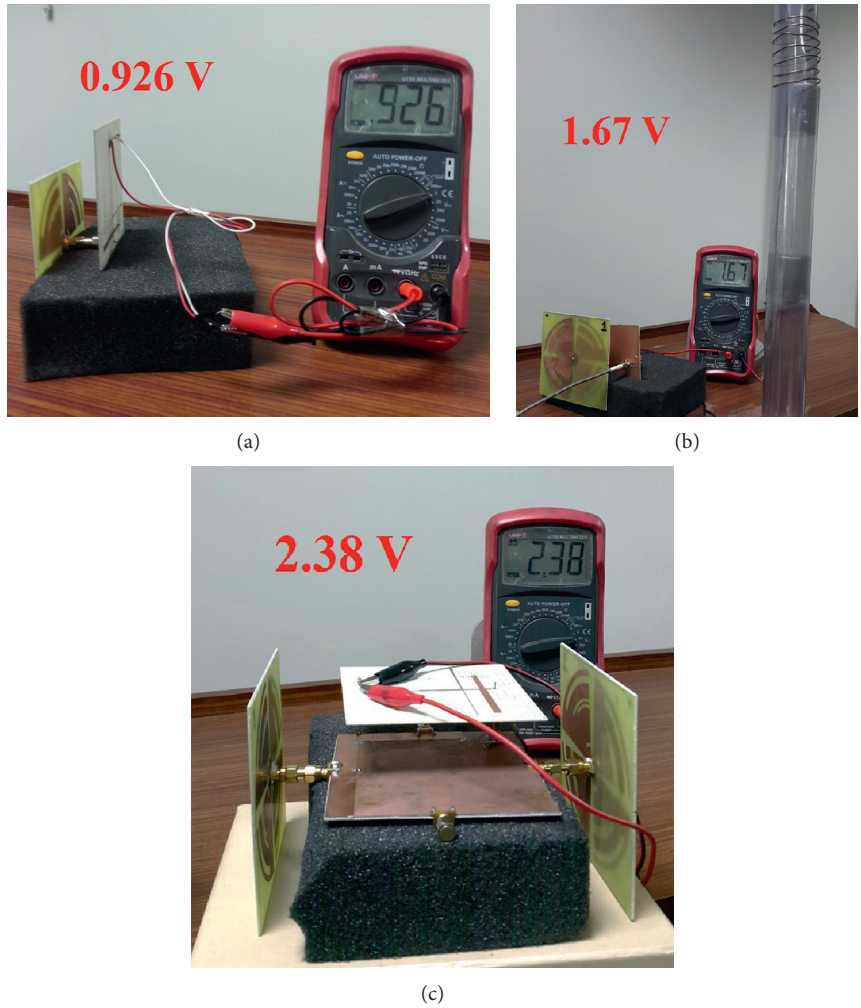

(a) (b)

(c)

Figure 32: Dedicated testing setup for the rectenna at −10 dBm input power using (a) single multiband antenna element, (b) single multiband antenna element combined with FM rectenna, and (c) two multiband antenna elements (all measurements have been conducted with multitone sources).

7.1. Dedicated Source Testing. A ~6.5 dBi log periodic antenna (LPDA) with a frequency range of 10 MHz–3 GHz is used as transmit antenna. It is connected to R&S SME06 signal generator to transmit varying powers at the desired frequencies. The rectenna module is placed in the far-field of the transmitting antenna.

The multiband antenna is initially connected to the R&S FS300 spectrum analyzer and the received RF power is noted. The distance between the proposed antenna and the source antenna is varied to calibrate input power levels between −40 and 0 dBm. Note that this power level refers to the power input to the rectifier. Next, the spectrum analyzer is replaced with direct connection of the proposed antenna to the rectifier circuit. The distance of the rectenna module from the source antenna is again varied to measure harvested voltage at different input power levels. The DC output voltage across the load resistance at different power levels is measured using a digital multimeter. The measured values of RF-DC conversion efficiency are found using (18) where the output DC power P_{DC} is found from the measured DC voltage using

$$P_{DC}\,(\text{dBm}) = 10\log\left(\frac{V_{DC}^2}{R_L} \times 10^3\right). \tag{19}$$

The energy harvested by the rectenna using a single antenna is shown in Figure 32(a). A Peak voltage of 0.926 V is harvested at an input power level of −10 dBm. Multiple RF sources have been used to generate signals of required frequencies (900, 1730, and 2400 MHz) at −10 dBm. Figure 32(b) shows the test setup of the multiband and FM rectenna using a dedicated source. It can be seen that the harvested voltage is considerably increased due to the addition of the FM band at a similar input power. This is because of the high efficiency of the multiband rectifier at FM frequencies. Figure 32(c) shows the test setup of the two multiband rectennas using a dedicated source. Due to the nonavailability of four signal generators, testing is carried out using only two multiband antennas of the proposed cube structure. One multitone source is placed in front of each antenna to establish an ambient environment with signal incident from all sides. The output rectified voltage is 2.38 V, which is more than double the voltage produced by rectenna using a single multiband antenna (Figure 32(a)). This proves that use of four antennas will roughly quadruple the voltage output. Similarly the FM antenna connected with the cubic rectenna will add to the output voltage. Theoretically the measured voltage should increase by a factor of 4 after doubling the number of antennas. However, due to the inherent losses of the power combiner and efficiency limitation of the rectifier, a lesser value (2.38 V) is practically achieved. It needs to be noted that all the results of harvested output voltage with dedicated sources are obtained while keeping the level of input power level at −10 dBm at all frequencies of interest. This has been done to maintain uniformity in measurements and due to limitations of signal source to achieve higher signal level. The constant power level was ensured by periodically changing the distance between the rectenna and the source antenna to achieve −10 dBm power at the input to the rectifier.

7.2. Ambient Testing. Rectenna testing is also carried out in a semiurban university campus. The testing site is approximately 300 m from the nearest cellular tower and 5 m from the nearest Wi-Fi source. The measured ambient power levels vary around −60 dBm to −15 dBm for the relevant frequency bands with an average power level of −15 dBm using the proposed antenna. Figure 33(a) shows the test setup of the proposed rectenna in the presence of ambient RF sources. The output voltage from the rectenna with a single antenna is recorded to be 92 mV. Ambient rectenna testing for the 3D cube structure is also carried out with and without the FM rectenna. The measurement setup for the cube with multiband antennas only is shown in Figure 33(b). An output voltage of 123 mV is obtained, which is higher as compared to that of the single multiband antenna. Figures 33(c) and 33(d) show the ambient testing setup for complete cubic rectenna including the FM rectenna. The output voltage obtained after deembedding the RF cable used for FM antenna is 315 mV, which is higher than the preceding cases. It is observed that the FM input significantly increases the harvested voltage even though the ambient power available in the FM band is lower than the communication bands, as discussed in Section 3. This increase in output voltage can be attributed to the high efficiency of FM rectifier as shown in Figure 31.

The average available power in the environment measured using the proposed antenna is nearly −15 dBm. The DC power harvested by the antenna is calculated to be −20.035 dBm using (19) where the DC voltage and load resistance are taken as 315 mV and 10 kΩ, respectively. Using (18), the overall conversion efficiency of the rectenna for ambient measurements is found as 31.3% at −15 dBm. This is the multitone efficiency and is therefore higher than individual efficiencies at each frequency band except the FM band. The results are in accordance with the simulated efficiency values of quad-band rectifier as shown in Figure 31. The degradation in overall efficiency is accounted by the losses incurred due to DC combination of two dissimilar rectennas.

7.3. Comparative Performance Analysis. A comparison of the proposed rectifier to the existing topologies is presented in Figure 34. The proposed triband rectifier is at least 10% more efficient than the designs reported in [10, 11, 13, 36] while there is a 40% improvement in the rectifier's efficiency at 2.4 GHz as compared to [20].

A tabular comparison between the proposed rectenna and some recent rectenna designs is given in Table 4. It can be seen that the proposed design is the only one that harvests energy from the FM band along with GSM900, GSM1800, and Wi-Fi bands. It not only miniaturizes the FM element but also integrates it into the overall structure. In addition, a hybrid combination of outputs and

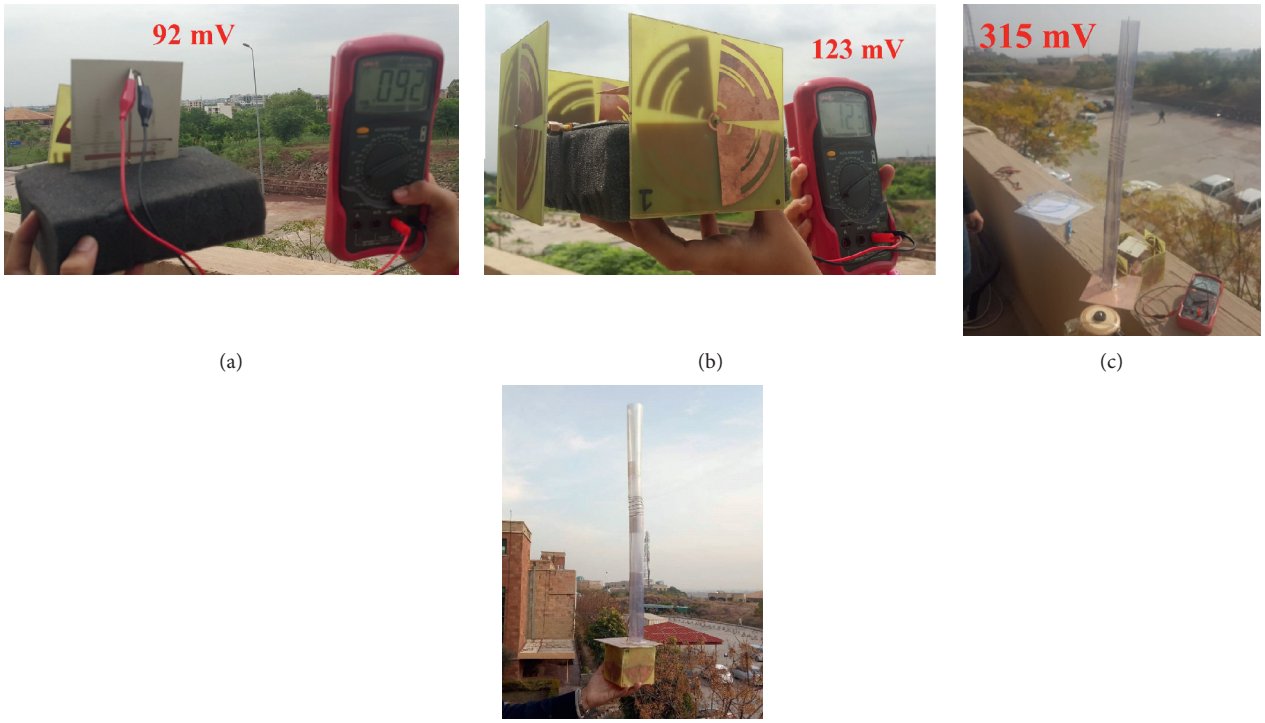

Figure 33: Ambient environment testing setup for the rectenna using (a) single multiband antenna element, (b) proposed cube rectenna without FM antenna, (c) proposed cube rectenna (open), and (d) proposed cube rectenna (closed).

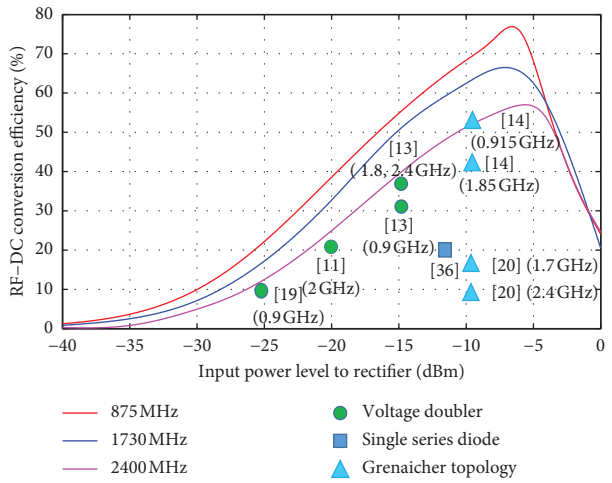

Figure 34: Comparison of conversion efficiency of proposed rectifier with existing topologies.

two antennas results in an output voltage as high as 2.38 V at an input power level of −10 dBm in dedicated mode. The rectenna also shows 315 mV harvested voltage in ambient settings with an average available power of −15 dBm in the environment. Although this voltage is not enough to power conventional IoT devices, the integration of boosting circuits and power management units with the rectenna module can greatly enhance the harvested voltage. The demonstration of powering an IoT sensor using the proposed rectenna in ambient settings is envisaged as a future extension to this work. Integration of multiple 3D mountable rectenna modules makes the proposed design a good candidate for energy harvesting for IoT applications.

Table 4: Comparison of the proposed rectenna with related designs.

Ref. (year)	Frequency (GHz)	Random polarization receiving capability	Type of matching network used	Input power level (dBm)	Maximum RF-DC conversion efficiency (%)	Maximum conversion efficiency at multitone input (%)	Maximum harvested DC output voltage (V)
[10] (2016)	Six-band 0.55, 0.75, 0.9, 1.85, 2.15, 2.45	Dual CP	Lumped matching for each band	−30 to −5	67 at −5 dBm	80 at −5 dBm	0.663 at −15 dBm
[11] (2018)	Triple-band 2.1, 2.4–2.48, 3.3–3.8	LP	Differential matching	−20 to 0	53 at −13 dBm	Not available	Not available
[12] (2017)	Broadband 0.9–1.1 and 1.8–2.5	Dual LP	Not used	−25 to 0	60 at 0 dBm	Not available	Not available
[13] (2015)	Four-band 0.9, 1.8, 2.1, 2.4	Dual LP	Lumped matching for each band	−20 to 6	84 at 5.8 dBm	84 at 5.8 dBm	0.9 at −15 dBm
[34] (2018)	Triband 0.9, 1.8 and 2.1	Linear	Optimization based TL matching	−35 to −10	56 at −10 dBm	55 at −10 dBm	0.75 at −10 dBm
[35] (2017)	Triband 0.9, 1.8 and 2.1	Linear	Optimization based TL matching	−30 to 10	40 at −10 dBm	81 with −30 dBm per tone	0.6 at 500 μW/m^2
[15] (2013)	FM band 81.9–84.7	Linear	Lumped element matching	NA	NA	Single tone input	1.72 at −20 dBm
[16] (2017)	FM band 88–108	Linear	Lumped element matching	−35 to 10	74 at 5 dBm	Single tone input	0.619 at 14.2 dBm
[17] (2019)	FM band 88–108	Linear	Lumped element matching	−20 to 10	56 at 0 dBm	Single tone input	1.5 at 0 dBm
This work (2019)	*Four-band 0.098, 0.9, 1.8, 2.4*	*Dual LP*	*Closed form equation based TL matching*	*−30 to 0*	*69 at −6 dBm*	*40 at −10 dBm*	*2.38 at −10 dBm*

8. Conclusions

A novel multiband 3D rectenna is proposed for RF energy harvesting using a modified cross-dipole antenna and a transmission line based triband matching network designed for multiple power levels and frequency bands using closed form equations. The rectenna achieves a maximum measured efficiency of 70% with −6 dBm input power at 98 MHz, whereas the ambient rectenna measurements show a maximum achieved efficiency of 31.3% at multitone inputs. It exhibits a comparable RF-DC conversion efficiency and a higher output DC voltage compared to recent published designs. Moreover, the design of the receiving antenna and the triband impedance matching network is based on closed form equations making it generic in nature and extendable to any desired frequency range. The 3D cubic structure enhances antenna gain and enables the rectenna to harvest greater amount of energy from all directions. This is the first published rectenna design that is capable of harvesting energy from the FM band along with GSM900, GSM1800, and Wi-Fi bands. The integration of multiple 3D mountable rectenna modules makes it suitable for powering IoT sensors in practical scenarios.

Data Availability

The data used to support the findings of this study are available from the corresponding author upon request.

Conflicts of Interest

The authors declare that there are no conflicts of interest regarding the publication of this paper.

Acknowledgments

This work was funded through Higher Education Commission (HEC), National Research Program for Universities (NRPU), Grant Program Project no. 9971, titled "RF Energy Harvesting for Internet of Things (IoT) Applications."

References

[1] W. Brown, "Experiments involving a microwave beam to power and position a helicopter," *IEEE Transactions on Aerospace and Electronic Systems*, vol. AES-5, no. 5, pp. 692–702, 1969.

[2] F. Congedo, G. Monti, L. Tarricone, and V. Bella, "A 2.45-GHz vivaldi rectenna for the remote activation of an end device radio node," *IEEE Sensors Journal*, vol. 13, no. 9, pp. 3454–3461, Sep. 2013.

[3] B. J. DeLong, A. Kiourti, and J. L. Volakis, "A radiating near-field patch rectenna for wireless power transfer to medical implants at 2.4 GHz," *IEEE Journal of Electromagnetics, RF and Microwaves in Medicine and Biology*, vol. 2, no. 1, pp. 64–69, 2018.

[4] B. Strassner and K. Kai Chang, "5.8-GHz circularly polarized dual-rhombic-loop traveling-wave rectifying antenna for low power-density wireless power transmission applications,"

IEEE Transactions on Microwave Theory and Techniques, vol. 51, no. 5, pp. 1548–1553, 2003.

[5] Q. Awais, Y. Jin, H. T. Chattha, M. Jamil, H. Qiang, and B. A. Khawaja, "A compact rectenna system with high conversion efficiency for wireless energy harvesting," *IEEE Access*, vol. 6, pp. 35 857–35 866, 2018.

[6] Y.-J. Ren and K. Chang, "5.8-GHz circularly polarized dual-diode rectenna and rectenna array for microwave power transmission," *IEEE Transactions on Microwave Theory and Techniques*, vol. 54, no. 4, pp. 1495–1502, 2006.

[7] Y. Yang, L. Li, J. Li et al., "A circularly polarized rectenna array based on substrate integrated waveguide structure with harmonic suppression," *IEEE Antennas and Wireless Propagation Letters*, vol. 17, no. 4, pp. 684–688, 2018.

[8] Y. Yang, J. Li, L. Li et al., "A 5.8 GHz circularly polarized rectenna with harmonic suppression and rectenna array for wireless power transfer," *IEEE Antennas and Wireless Propagation Letters*, vol. 17, no. 7, pp. 1276–1280, 2018.

[9] X. Li, L. Yang, and L. Huang, "Novel design of 2.45-GHz rectenna element and array for wireless power transmission," *IEEE Access*, vol. 7, pp. 28356–28362, 2019.

[10] C. Song, Y. Huang, P. Carter et al., "A novel six-band dual cp rectenna using improved impedance matching technique for ambient rf energy harvesting," *IEEE Transactions on Antennas and Propagation*, vol. 64, no. 7, pp. 3160–3171, 2016.

[11] S. Chandravanshi, S. S. Sarma, and M. J. Akhtar, "Design of triple band differential rectenna for RF energy harvesting," *IEEE Transactions on Antennas and Propagation*, vol. 66, no. 6, pp. 2716–2726, 2018.

[12] C. Song, Y. Huang, J. Zhou et al., "Matching network elimination in broadband rectennas for high-efficiency wireless power transfer and energy harvesting," *IEEE Transactions on Industrial Electronics*, vol. 64, no. 5, pp. 3950–3961, 2017.

[13] V. Kuhn, C. Lahuec, F. Seguin, and C. Person, "A multi-band stacked rf energy harvester with RF-to-DC efficiency up to 84%," *IEEE Transactions on Microwave Theory and Techniques*, vol. 63, no. 5, pp. 1768–1778, 2015.

[14] C. Song, Y. Huang, J. Zhou, J. Zhang, S. Yuan, and P. Carter, "A high-efficiency broadband rectenna for ambient wireless energy harvesting," *IEEE Transactions on Antennas and Propagation*, vol. 63, no. 8, pp. 3486–3495, 2015.

[15] A. Noguchi and H. Arai, "Small loop rectenna for rf energy harvesting," in *Proceedings of the 2013 Asia-Pacific Microwave Conference Proceedings (APMC)*, pp. 86–88, IEEE, Seoul, South Korea, November 2013.

[16] Mutee-Ur-Rehman, M. I. Qureshi, W. Ahmad, and W. T. Khan, "Radio frequency energy harvesting from ambient fm signals for making battery-less sensor nodes for wireless sensor networks," in *Proceedings of the 2017 IEEE Asia Pacific Microwave Conference (APMC)*, pp. 487–490, Kuala Lumpur, Malaysia, November 2017.

[17] E. M. Jung, Y. Cui, T.-H. Lin et al., "A wideband, quasi-isotropic, kilometer-range fm energy harvester for perpetual IoT," *IEEE Microwave and Wireless Components Letters*, vol. 30, no. 2, pp. 201–204, 2020.

[18] J. Liu, X. Y. Zhang, and C.-L. Yang, "Analysis and design of dual-band rectifier using novel matching network," *IEEE Transactions on Circuits and Systems II: Express Briefs*, vol. 65, no. 4, pp. 431–435, 2018.

[19] J.-J. Lu, X.-X. Yang, H. Mei, and C. Tan, "A four-band rectifier with adaptive power for electromagnetic energy harvesting," *IEEE Microwave and Wireless Components Letters*, vol. 26, no. 10, pp. 819–821, 2016.

[20] C.-Y. Hsu, S.-C. Lin, and Z.-M. Tsai, "Quadband rectifier using resonant matching networks for enhanced harvesting capability," *IEEE Microwave and Wireless Components Letters*, vol. 27, no. 7, pp. 669–671, 2017.

[21] X. Liu, Y. Liu, S. Li, F. Wu, and Y. Wu, "A three-section dual-band transformer for frequency-dependent complex load impedance," *IEEE Microwave and Wireless Components Letters*, vol. 19, no. 10, pp. 611–613, 2009.

[22] U. Olgun, C.-C. Chi-Chih Chen, and J. L. Volakis, "Investigation of rectenna array configurations for enhanced rf power harvesting," *IEEE Antennas and Wireless Propagation Letters*, vol. 10, pp. 262–265, 2011.

[23] T. Matsunaga, E. Nishiyama, and I. Toyoda, "5.8-GHz stacked differential rectenna suitable for large-scale rectenna arrays with dc connection," *IEEE Transactions on Antennas and Propagation*, vol. 63, no. 12, pp. 5944–5949, 2015.

[24] Spotloght solar, "solar energy trees" https://spotlightsolar.com/solar-energy-trees-projects.

[25] New world wind, "the wind tree" https://newworldwind.com/en/wind-tree/.

[26] F. Khalid, M. U. Khan, N. Shoaib, W. Saeed, and H. M. Cheema, "Multiband antenna design for ambient energy harvesting based on rf field investigation," in *Proceedings of the 2018 IEEE International Symposium on Antennas and Propagation & USNC/URSI National Radio Science Meeting*, pp. 673-674, Boston, MA, USA, July 2018.

[27] H. H. Tran and I. Park, "Wideband circularly polarized cavity-backed asymmetric crossed bowtie dipole antenna," *IEEE Antennas and Wireless Propagation Letters*, vol. 15, pp. 358–361, 2016.

[28] T. K. Nguyen, H. H. Tran, and N. Nguyen-Trong, "A wideband dual-cavity-backed circularly polarized crossed dipole antenna," *IEEE Antennas and Wireless Propagation Letters*, vol. 16, pp. 3135–3138, 2017.

[29] S. X. Ta, H. Choo, I. Park, and R. W. Ziolkowski, "Multi-band, wide-beam, circularly polarized, crossed, asymmetrically barbed dipole antennas for gps applications," *IEEE Transactions on Antennas and Propagation*, vol. 61, no. 11, pp. 5771–5775, 2013.

[30] M.-T. Wu and M.-L. Chuang, "Application of transmission-line model to dual-band stepped monopole antenna designing," *IEEE Antennas and Wireless Propagation Letters*, vol. 10, pp. 1449–1452, 2011.

[31] R. C. Hansen, "Optimum inductive loading of short whip antennas," *IEEE Transactions on Vehicular Technology*, vol. 24, no. 2, pp. 21–29, 1975.

[32] W. Saeed, N. Shoaib, H. M. Cheema, M. U. Khan, and F. Khalid, "Triband impedance transformer for frequency dependent complex load," in *Proceedings of the 18th International Symposium on Antenna Technology and Applied Electromagnetics (ANTEM)*, pp. 1–3, Waterloo, ON, Canada, August 2018.

[33] M. A. Maktoomi, M. S. Hashmi, A. P. Yadav, and V. Kumar, "A generic tri-band matching network," *IEEE Microwave and Wireless Components Letters*, vol. 26, no. 5, pp. 316–318, 2016.

[34] A. Bakytbekov, T. Q. Nguyen, C. Huynh, K. N. Salama, and A. Shamim, "Fully printed 3d cube-shaped multiband fractal rectenna for ambient rf energy harvesting," *Nano Energy*, vol. 53, pp. 587–595, 2018.

[35] S. Shen, C.-Y. Chiu, and R. D. Murch, "A dual-port triple-band l-probe microstrip patch rectenna for ambient rf energy harvesting," *IEEE Antennas and Wireless Propagation Letters*, vol. 16, pp. 3071–3074, 2017.

[36] M. Pinuela, P. D. Mitcheson, and S. Lucyszyn, "Ambient RF energy harvesting in urban and semi-urban environments," *IEEE Transactions on Microwave Theory and Techniques*, vol. 61, no. 7, pp. 2715–2726, 2013.